arXiv:2107.02190v2 [astro-ph.CO] 15 Mar 2022

Constraining primordial black holes as dark matter using the global 21-cm signal with X-ray heating and excess radio background

Shikhar Mittal[ID]**, Anupam Ray**[ID]**, Girish Kulkarni**[ID]**, and Basudeb Dasgupta**[ID]

Tata Institute of Fundamental Research, Homi Bhabha Road, Mumbai 400005, India

E-mail: shikhar.mittal@tifr.res.in, anupam.ray@theory.tifr.res.in, kulkarni@theory.tifr.res.in, bdasgupta@theory.tifr.res.in

Abstract. Using the global 21-cm signal measurement by the EDGES collaboration, we derive constraints on the fraction of the dark matter that is in the form of primordial black holes (PBHs) with masses in the range 10^{15}–10^{17} g. Improving upon previous analyses, we consider the effect of the X-ray heating of the intergalactic medium on these constraints, and also use the full shape of the 21-cm absorption feature in our inference. In order to account for the anomalously deep absorption amplitude, we also consider an excess radio background motivated by LWA1 and ARCADE2 observations. Because the heating rate induced by PBH evaporation evolves slowly, the data favour a scenario in which PBH-induced heating is accompanied by X-ray heating. Also, for the same reason, using the full measurement across the EDGES observation band yields much stronger constraints on PBHs than just the redshift of absorption. We find that 21-cm observations exclude $f_{\mathrm{PBH}} \gtrsim 10^{-9.7}$ at 95% CL for $M_{\mathrm{PBH}} = 10^{15}$ g. This limit weakens approximately as M_{PBH}^4 towards higher masses, thus providing the strongest constraints on ultralight evaporating PBHs as dark matter over the entire mass range 10^{15}–10^{17} g. Under the assumption of a simple spherical gravitational collapse based on the Press-Schechter formalism, we also derive bounds on the curvature power spectrum at extremely small scales ($k \sim 10^{15} \, \mathrm{Mpc}^{-1}$). This highlights the usefulness of global 21-cm measurements, including non-detections, across wide frequency bands for probing exotic physical processes.

Keywords: physics of the early universe; high redshift galaxies; primordial black holes; dark matter theory

Contents

1   Introduction

The 21-cm signal — the brightness temperature of the 1420.4 MHz hyperfine transition of cosmological neutral hydrogen measured against the cosmic microwave background (CMB) temperature — has been proposed as a probe of Cosmic Dawn and the Epoch of Reionization (EoR) [1]. Observing this signal is a challenging task due to large foregrounds, mainly the galactic synchrotron radiation [2–5]. In 2018, the EDGES collaboration (Experiment to Detect the Global EoR Signal) [6] reported the first and till-date the only measurement of the cosmological 21-cm signal [7]. The key features of this absorption signal are its location (78.2 MHz, corresponding to $z = 17.2$), amplitude ($\Delta T_{\rm b} \approx -500\,{\rm mK}$) and the full width at half maximum (19 MHz). The most interesting and intriguing part of their detected signal is the amplitude, which is found to be more than double the prediction of even the most optimistic theoretical models.

    The spin temperature of the hyperfine energy states of neutral hydrogen (H I) is the main quantity that decides the amplitude of the 21-cm signal. At redshifts $z \lesssim 30$, the physics of the spin temperature is expected to be relatively simple. At these redshifts, it is mainly affected by the standard physics of H I and Lyman-α (Ly α) interaction via the Wouthuysen-Field effect [8, 9]. Other relevant processes are the adiabatic cooling of the intergalactic medium (IGM) and small heating effects due the Ly α radiation [10–13] and the ambient 21-cm background [14]. The shape of the absorption signal measured by EDGES is potentially also decided by processes such as Compton heating [15], X-ray heating [16–19] and reionization [20, 21]. The disagreement between models that include these ingredients and the EDGES measurement has inspired many new models. These explain the large amplitude using

either an excess cooling of ordinary baryonic matter [22–25] or an excess radiowave background (ERB) [26, 27].

The motivation for the latter idea is the recently-confirmed excess radio brightness above the CMB by the Long Wavelength Array (LWA1) [28] for frequencies 40–80 MHz. This excess was first detected by Absolute Radiometer for Cosmology, Astrophysics and Diffuse Emission (ARCADE 2) [29]. While the origin of this excess radio background is not very well understood [30], it still provides an empirically plausible means of explaining the EDGES result.

Beyond these modelling efforts that aim to understand the EDGES result are the attempts to use the EDGES result for constraining various physical processes. Thanks to the richness of 21-cm physics, several studies on 21-cm signal have been theorised (many of which have existed even before the EDGES detection) to be useful to probe primordial magnetic fields [31–36], gravitational waves [37–39], warm dark matter [40–44], dark matter decay and annihilation [45–48], viscous dark matter [49] and many other exotic processes. We address one such possibility in this paper by considering the effect of primordial black holes (PBHs) on the 21-cm signal and deriving constraints on the abundance of PBHs from the EDGES measurement.

Understanding the constituents of dark matter (DM) is one of the major problems in cosmology. Primordial black holes, possibly formed due to the collapse of large density perturbations in the very early Universe [50–53], can partly or even entirely explain the present day DM density [54–58]. Ultralight evaporating PBHs, i.e., PBHs in the mass range of 10^{15}–10^{17} g are typically probed via observations of their evaporation products. Non-observations of such Hawking radiated photons [59–64], neutrinos [58], and electrons/positrons [58, 65–68] in various space- as well as ground-based detectors provide stringent exclusion limits on the fraction of DM composed of ultralight evaporating PBHs. PBHs in these mass range can also be constrained via precise measurements of the CMB [69–73], dwarf galaxy heating [74, 75], and radio observations [76, 77]. Observations of low energy ($\sim$ MeV) photons from the Galactic Centre by the upcoming soft gamma-ray telescopes such as AMEGO, as well as next-generation neutrino detectors can also project stringent exclusion limits on the fraction of DM composed of ultralight evaporating PBHs [78–81]. The measurement of the 21-cm signal is considered to be another promising probe that can be used to constrain the DM fraction of PBHs in various mass windows [82–89]. Recently, by using the EDGES measurement, Clark et al. (2018) [84] showed that evaporating PBHs in the mass range of 10^{15}–10^{17} g cannot form the solitary component of DM.

In this paper, we revisit 21-cm constraints on the PBH abundance and aim to improve upon previous work [84] in two significant ways. Firstly, we use a more sophisticated model of all the known astrophysical phenomena that affect the 21-cm signal. This includes processes such as X-ray heating, Ly α heating, and an ERB that were neglected in previous work, but can nonetheless have a significant impact on the inferred PBH constraints. Secondly, and more importantly, we aim to utilise all of the information contained in the EDGES measurement in our analysis. Previously published analysis [84] only used a central location of the 21-cm absorption feature. In this work we use the full EDGES data for $28 \gtrsim z \gtrsim 14$, rather than just at a specific redshift, thus capturing all features of the observed signal. We use an MCMC-enabled Bayesian analysis to derive our constraints. This also allows us to study the covariance of PBH parameters with other processes affecting the 21-cm signal.

This paper is organized as follows. In section 2, we describe our model of the 21-cm signal. Section 3 discusses the effect of PBHs on the 21-cm signal. We describe our inference procedure in section 4. Our results are presented in section 5. We discuss the implications of our results and some caveats in section 6, and end with a summary in section 7. The following cosmological parameters are used: $\Omega_{\rm m} = 0.315$, $\Omega_{\rm b} = 0.049$, $\Omega_{\Lambda} = 0.685$, $h = 0.674$, $Y_{\rm p} = 0.245$, $T_0 = 2.725\,{\rm K}$, $\sigma_8 = 0.811$ and $n_{\rm s} = 0.965$ [90, 91], where T_0 and $Y_{\rm p}$ are the CMB temperature measured today and primordial helium fraction by mass, respectively.

2 The global 21-cm signal

The global (sky-averaged) 21-cm signal is the 21-cm brightness measured against the background (CMB or CMB+ERB, as in this work). Because of the long wavelength, the intensities can be

written in terms of temperatures using the Rayleigh-Jeans law giving rise to a 'differential brightness temperature' for the global 21-cm signal [92–96], given by

$$\Delta T_{\rm b} = 27 \bar{x}_{\rm HI} \left(\frac{1 - Y_{\rm p}}{0.76} \right) \left(\frac{\Omega_{\rm b} h^2}{0.023} \right) \sqrt{\frac{0.15}{\Omega_{\rm m} h^2} \frac{1+z}{10}} \left(1 - \frac{T_{\rm r}}{T_{\rm s}} \right) {\rm mK} \,, \tag{2.1}$$

where $x_{\rm HI}$ is the neutral hydrogen fraction, $T_{\rm s}$ is the spin temperature, and $T_{\rm r}$ is the net background temperature.

The spin temperature is not a real thermodynamic quantity but only an effective excitation temperature that quantifies the relative population of the hyperfine levels [97]. The processes affecting these populations and hence the spin temperature are the three Einstein processes, the Wouthuysen-Field effect [8, 9], and the collision of hydrogen atoms with free electrons and other hydrogen atoms. Detailed balance between these processes then gives us the spin temperature

$$T_{\rm s}^{-1} = \frac{x_{\rm r} T_{\rm r}^{-1} + (x_{\rm k} + x_\alpha) T_{\rm k}^{-1}}{x_{\rm r} + x_{\rm k} + x_\alpha} \,, \tag{2.2}$$

where $x_{\rm r}$, $x_{\rm k}$ and x_α are the 21-cm, collisional and Ly α coupling, respectively. Because of a near thermal equilibrium of gas and Ly α photons, we have made an assumption that the colour temperature is equal to the gas kinetic temperature, i.e. $T_\alpha \approx T_{\rm k}$ [9]. The modelling of hyperfine line couplings, $x_{\rm r}$, $x_{\rm k}$ and x_α, is discussed in section 2.1, and that for the evolution of the gas kinetic temperature $T_{\rm k}$ is given in section 2.2, where we outline our model for X-ray heating and Ly α heating that were previously ignored.

In eq. (2.1), $x_{\rm HI}$ is the neutral hydrogen fraction. The bar represents a global average over the cosmic volume, which includes H I and H II regions. However, in this work we will work at redshifts where the effects of reionization are unimportant, in which case the ionized volume fraction of H II region is always zero, i.e., $Q_{\rm HII} = 0$. This simplifies the calculation of $\bar{x}_{\rm HI}$ and we write [17, 98]

$$\bar{x}_{\rm HI} = (1 - Q_{\rm HII})(1 - x_{\rm e}) = 1 - x_{\rm e} \,, \tag{2.3}$$

where $x_{\rm e}$ is the electron fraction defined as the number density of electrons relative to total hydrogen

$$x_{\rm e} \equiv \frac{n_{\rm e}}{n_{\rm H}} \,. \tag{2.4}$$

in the IGM. We discuss our model for $x_{\rm e}$ in section 2.3.

The background temperature $T_{\rm r}$ includes the standard contribution from the CMB as well as a possible ERB, as we discuss in section 2.4.

2.1 Hyperfine line couplings

We now discuss our models for the hyperfine line couplings, $x_{\rm r}$, $x_{\rm k}$ and x_α.

2.1.1 21-cm coupling

The 21-cm coupling is given by [14]

$$x_{\rm r} = \frac{1 - e^{-\tau_{\rm 21cm}}}{\tau_{\rm 21cm}} \,, \tag{2.5}$$

where

$$\tau_{\rm 21cm} = \frac{3}{32\pi} \frac{A_{10}}{H} n_{\rm HI} \lambda_{\rm 21cm}^3 \frac{T_*}{T_{\rm s}} \,, \tag{2.6}$$

is the 21-cm optical depth [e.g., 99]. Because $T_{\rm s}$ and $x_{\rm r}$ are dependent on each other, we may find their values iteratively as follows [27]:

1. Set $x_{\rm r} = 1$

2. Evaluate $T_{\rm s}$ using eq. (2.2)

3. Using T_s evaluated in step 2, find the new x_r using eqs. (2.5) and (2.6)

4. Repeat from step 2 using an updated x_r found in step 3

The convergence is rapid and usually 3 iterations are sufficient. The resultant value of x_r is usually close to 1.

2.1.2 Collisional coupling

Collisions can cause hyperfine transition in a neutral hydrogen atom via two different mechanisms: (a) by spin exchange in which collisions with other hydrogen atoms, electrons, or protons swap the electron with another that has the opposite spin, or (b) by spin flip of the electron via magnetic forces. Process (a) is more likely to occur [92]. The collisional coupling is

$$x_k = \frac{T_* C_{10}}{T_r A_{10}},$$ (2.7)

where C_{10} is the de-excitation rate by collisions and $A_{10} = 2.85 \times 10^{-15}$ Hz is the Einstein coefficient of spontaneous emission for the hyperfine transition [100] and $T_* = h_P \nu_{21cm}/k_B$ for Planck's constant h_P and Boltzmann constant k_B. Collisional de-excitation rate is expressed as

$$C_{10} = n_{HI}\kappa_{HH} + n_e \kappa_{eH} + n_p \kappa_{pH},$$ (2.8)

where n_i is the number density of species i and κ_{iH} is the reaction rate, in units of volume per unit time, between i and H I. Several papers [92, 101–103] have tabulated these rates at different temperatures. Useful fitting functions exist in literature which fit the data given in these tables. They are as follows [104, 105]:

$$\log_{10} \kappa_{eH} = \begin{cases} -15.607 + \frac{1}{2}\log_{10} T_k \cdot \exp\left[-(\log_{10} T_k)^{4.5}/1800\right] \text{ if } T_k < 10^4 \\ -14.102 \text{ if } T_k \geqslant 10^4, \end{cases}$$ (2.9)

and

$$\kappa_{HH} = 3.1 \times 10^{-17} T_k^{0.357} e^{-32/T_k}.$$ (2.10)

No fitting function for κ_{pH} is available in the literature. We therefore construct and use the fit

$$\kappa_{pH} = 10^{-16} \left[c_0 + c_1 \log_{10} T_k + c_2 \log_{10}^2 T_k + c_3 \log_{10}^3 T_k\right],$$ (2.11)

where $c_0 = 4.28, c_1 = 0.24, c_2 = -1.37$ and $c_3 = 0.53$ for the available data [106]. All κ_{iH}s are in m^{3}s^{-1}. The final expression of x_k can be written as

$$x_k = \frac{T_* n_H}{T_r A_{10}} \left[(1 - x_e)\kappa_{HH} + x_e \kappa_{eH} + x_e \kappa_{pH}\right],$$ (2.12)

where we have used the charge neutrality of the Universe by which $n_e = n_p$.

2.1.3 Ly α coupling

The Ly α photons produced by the first galaxies indirectly affect the spin temperature through a process known as the Wouthuysen-Field effect [8, 9]. Accurate modelling of this coupling is essential at Cosmic Dawn since it is the Ly α coupling that makes the 21-cm signal observable. The expression for the Ly α coupling can be written as

$$x_\alpha = (1 - \delta_\alpha)\frac{J_\alpha}{J_0},$$ (2.13)

where δ_α represents a distortion in the Ly α background due to its interaction with neutral hydrogen atom [13]

$$\delta_\alpha = {}_3F_0(1/3, 2/3, 1; 0; -\xi_1),$$ (2.14)

for

$$\xi_1 = \frac{9\pi}{4a\tau_\alpha\eta^3} \,, \tag{2.15}$$

and $_3F_0$ being the $(3,0)$-hypergeometric function [107]. The Voigt parameter [108], the Ly α optical depth [109] and the recoil parameter [10] are given by

$$a = \frac{A_\alpha}{4\pi\nu_\alpha}\sqrt{\frac{m_{\rm H}c^2}{2k_{\rm B}T_{\rm k}}} \,, \tag{2.16a}$$

$$\tau_\alpha = \frac{3}{8\pi}\frac{A_\alpha}{H}n_{\rm HI}\lambda_\alpha^3 \,, \tag{2.16b}$$

$$\eta = \frac{h_{\rm P}/\lambda_\alpha}{\sqrt{2m_{\rm H}k_{\rm B}T_{\rm k}}} \,, \tag{2.16c}$$

respectively. Here $A_\alpha = 6.25 \times 10^8\,{\rm Hz}$ is the Einstein spontaneous emission coefficient of Ly α transition, $m_{\rm H}$ is the mass of hydrogen, $\lambda_\alpha(\nu_\alpha)$ is the wavelength (frequency) of the Ly α photon, and c is the speed of light.

The factor J_0 is a combination of fundamental constants and background temperature [13]

$$J_0 = 5.54 \times 10^{-8}\frac{T_{\rm r}}{T_0}\,{\rm m}^{-2}\,{\rm s}^{-1}\,{\rm Hz}^{-1}\,{\rm sr}^{-1} \,. \tag{2.17}$$

To calculate the undisturbed Ly α specific intensity far from the resonance line, J_α, we need the comoving emissivity. The latter is defined as the number of photons emitted per unit comoving volume per unit proper time per unit energy at redshift z and energy E. It can be constructed based on the approach taken in ref. [99]. We choose Population II type star as our base model for spectral energy distribution (SED, number of photons emitted per unit energy per baryon). It is given by [13]

$$\phi_\alpha(E) = \begin{cases} 2902.91\,\hat{E}^{-0.86} & \text{if } E \in [E_\alpha, E_\beta] \\ 1303.34\,\hat{E}^{-7.66} & \text{if } E \in (E_\beta, E_\infty] \,, \end{cases} \tag{2.18}$$

in eV^{-1}, where $\hat{E} = E/E_\infty$, $E_\alpha = 10.2\,{\rm eV}$, $E_\beta = 12.09\,{\rm eV}$ and $E_\infty = 13.6\,{\rm eV}$ are the energies corresponding to Ly α, Ly β and Lyman limit transition, respectively.

We can now write the comoving emissivity as

$$\epsilon_\alpha(E, z) = f_\alpha\phi_\alpha(E)\frac{\dot{\rho}_\star(z)}{m_{\rm b}} \,, \tag{2.19}$$

where $\dot{\rho}_\star$ is the comoving star formation rate density (SFRD) and $m_{\rm b}$ is the number-averaged baryon mass given as [110]

$$m_{\rm b} = \frac{m_{\rm H}n_{\rm H} + m_{\rm He}n_{\rm He} + m_{\rm e}n_{\rm e}}{n_{\rm H} + n_{\rm He} + n_{\rm e}} \,. \tag{2.20}$$

Neglecting the mass of electron and using

$$x_{\rm He} \equiv \frac{n_{\rm He}}{n_{\rm H}} = \frac{Y_{\rm p}}{4(1 - Y_{\rm p})} \,, \tag{2.21}$$

which is number density of helium relative to hydrogen, we get

$$m_{\rm b} = \frac{4m_{\rm H}}{4 - 3Y_{\rm p} + 4x_{\rm e}(1 - Y_{\rm p})} \,. \tag{2.22}$$

Since $x_{\rm e}$ is quite small, typically $\sim \mathcal{O}(10^{-3})$ for the redshift range considered in this work, we can write $m_{\rm b} \approx 1.22m_{\rm H}$.

The comoving SFRD, represented by $\dot{\rho}_\star(z)$, and measured in mass per unit time per unit comoving volume, is set by the rate at which baryons collapse into dark matter haloes [99]. We will

assume that only haloes of virial temperatures (T_{vir}) above a certain given value will contribute. Their number at a given redshift can be determined by the Press-Schechter formalism [111]. Thus,

$$\dot{\rho}_{\star}(z) = -f_{\star}\bar{\rho}_{\text{b}}^0(1+z)H(z)\frac{\mathrm{d}F_{\text{coll}}(z)}{\mathrm{d}z}\,, \tag{2.23}$$

where

$$\bar{\rho}_{\text{b}}^0 = \frac{3H_0^2}{8\pi G_{\text{N}}}\Omega_{\text{b}}\,, \tag{2.24}$$

is the mean cosmic baryon mass density measured today (H_0 is the Hubble's constant measured today and G_{N} is the Newton's gravitational constant), $f_{\star}$ is the star formation efficiency, defined as the fraction of baryons converted into stars in the haloes. Because it is completely degenerate with f_{α} and f_{X} (to be introduced in section 2.2.3) it does not matter what value we choose for it. Here we take the value from the fiducial set of parameters for Pop II stars from ref. [16], i.e. $f_{\star} = 0.1$. We denote the fraction of baryons that have collapsed into dark matter haloes by F_{coll}, given by [112]

$$F_{\text{coll}}(z) = \text{erfc}\left[\frac{\delta_{\text{crit}}(z)}{\sqrt{2}\sigma(m_{\text{min}})}\right]\,, \tag{2.25}$$

where erfc($\cdot$) represents the complementary error function, δ_{crit} is the linear critical density of collapse and σ^2 is the variance in smoothed density field. The minimum virial temperature enters the model through the expression of minimum halo mass for star formation, i.e.,

$$m_{\text{min}} = 10^8\frac{1}{\sqrt{\Omega_{\text{m}}h^2}}\text{M}_{\odot}\left[\frac{10}{1+z}\frac{0.6}{\mu}\frac{\min(T_{\text{vir}})}{1.98\times 10^4}\right]^{3/2}\,, \tag{2.26}$$

where h is the Hubble's constant measured today in units of $100\,\text{km}\,\text{s}^{-1}\,\text{Mpc}^{-1}$ and $\mu \approx 1.22$ [113]. We calculate $\delta_{\text{crit}}(z)/\sigma(m_{\text{min}})$ using COLOSSUS[1] [114]. As an example, for our cosmological parameters and $\min(T_{\text{vir}}) = 10^4\,\text{K}$ we get $F_{\text{coll}}(z=0) \approx 0.735$.

We treat the minimum $\log_{10}T_{\text{vir},4}$, which is a shorthand for $\log_{10}[T_{\text{vir}}/(10^4\,\text{K})]$, as a free parameter, and vary it between -0.75 and 1.25. For base model we take it to be 0, which corresponds to the atomic cooling threshold [112]. Our choice of the range is justified as it covers a large range of possible 21-cm signal values. See figure 1 for effect of changing this parameter on gas kinetic temperature and the 21-cm signal.

We scale the Ly α background up and down using the parameter f_{α}. Since we are uncertain about the SED or the SFRD of the galaxies, we set up a basic conservative model and vary it using f_{α}. In this work we vary it between 0.01 and 100 (cf. ref. [13]) with the base value at 1. Figure 1 shows the effect of varying this parameter on the 21-cm signal.

We can now evaluate J_{α} from ϵ_{α} (after internally converting ϵ_{α} from per unit energy basis to per unit frequency basis) as

$$J_{\alpha}(z) = \frac{c}{4\pi}(1+z)^2\sum_{n=2}^{23}P_n\int_z^{z_{\text{max}}}\frac{\epsilon_{\alpha}(E_n',z')}{H(z')}\,\mathrm{d}z'\,, \tag{2.27}$$

in units of number per unit time per unit area per unit frequency per unit solid angle. The nth term in the sum accounts for the finite probability P_n with which a photon in the upper Lyman line will redshift to Ly α wavelength. The values of P_n are computed in an iterative fashion using the selection rule and the decay rates. The detailed procedure and table of values can be found in refs. [115, 116]. The redshifted energy of nth Lyman series line is given by

$$E_n' = E_n\frac{1+z'}{1+z}\,, \tag{2.28}$$

---

[1]https://bitbucket.org/bdiemer/colossus/src/master/

where E_n is the energy of the photon released in transition from n^{th} state to ground state

$$E_n = 13.6\left(1 - \frac{1}{n^2}\right)\text{eV}\,. \tag{2.29}$$

The maximum redshift from which this photon could have been received is given by

$$1 + z_{\text{max}} = \frac{E_{n+1}}{E_n}(1+z) = \frac{1-(1+n)^{-2}}{1-n^{-2}}(1+z)\,. \tag{2.30}$$

2.2 Gas kinetic temperature and heating processes

The evolution of the gas kinetic temperature is also important in setting the amplitude of the 21-cm signal through the spin temperature (eq. 2.2). This is given by [13]

$$(1+z)\frac{\mathrm{d}T_{\text{k}}}{\mathrm{d}z} = 2T_{\text{k}} - \frac{T_{\text{k}}(1+z)}{1+x_{\text{He}}+x_{\text{e}}}\frac{\mathrm{d}x_{\text{e}}}{\mathrm{d}z} - \frac{2}{3n_{\text{b}}k_{\text{B}}H}\sum q\,, \tag{2.31}$$

where $n_{\text{b}} = n_{\text{H}}(1+x_{\text{He}}+x_{\text{e}})$ is the total particle number density. The first term on the right hand side of eq. (2.31) is the adiabatic cooling term because of an adiabatically expanding Universe, second term accounts for the change in internal energy due to changing particle number, and finally the third term is the sum of all heating and cooling processes. In this work we consider Compton, Ly α, Hawking radiation (HR), and X-ray heating. They are discussed one by one next. We must couple eq. (2.31) with an equation for the variation of x_{e}. The latter is discussed in section 2.3. The redshifts of our interest range from $1+z = 60$ to $1+z = 14$ with the initial condition, obtainable from RECFAST,[2] being $x_{\text{e}} \approx 2.47 \times 10^{-4}$ and $T_{\text{k}} \approx 70.28\,\text{K}$ at $1+z = 60$.

2.2.1 Compton heating

After recombination, the inverse Compton scattering of electrons off the background photons couples the matter and background radiation for $z \gtrsim 200$. Because of this Compton heating the temperature of matter and the background fall together as $(1+z)$ at these redshifts. As the Universe expands and becomes neutral Compton heating ceases to play any role [117, 118]. However, because of partial X-ray ionization of IGM in later times, $z \lesssim 60$, it may have a finite contribution, although only a minor one. The Compton heating term is [15]

$$\frac{2q_{\text{Comp}}}{3n_{\text{b}}k_{\text{B}}H} = \frac{32\sigma_{\text{T}}\sigma_{\text{S}}T_{\gamma}^4}{3Hm_{\text{e}}c^2}\frac{1}{1+x_{\text{He}}+x_{\text{e}}}(T_{\gamma} - T_{\text{k}})\,, \tag{2.32}$$

where $T_{\gamma} = T_0(1+z)$ is the CMB temperature at a redshift z, $\sigma_{\text{T}} = 6.65 \times 10^{-29}\,\text{m}^2$ is the Thomson scattering cross section and $\sigma_{\text{S}} = 5.67 \times 10^{-8}\,\text{Wm}^{-2}\text{K}^{-4}$ is the Stephan-Boltzmann constant.

2.2.2 Ly α heating

The other heating process we will consider here is the Ly α heating [13], which is a 'side effect' of Ly α coupling. Following our previous work [13], the term to be added in eq. (2.31) is

$$\frac{2q_{\alpha}}{3n_{\text{b}}k_{\text{B}}H} = \frac{8\pi}{3}\frac{h_{\text{P}}}{\lambda_{\alpha}^2}\sqrt{\frac{2T_{\text{k}}}{m_{\text{H}}k_{\text{B}}}}\frac{J_{\alpha}}{n_{\text{b}}}\left(I_{\text{c}} + \frac{J_{\alpha}^{\text{i}}}{J_{\alpha}^{\text{c}}}I_{\text{i}}\right)\,. \tag{2.33}$$

where I_{c} is the integral over the spectrum of continuum photons given as [12]

$$I_{\text{c}} = \eta(2\pi^4 a^2\tau_{\alpha}^2)^{1/3}\left[\text{Ai}^2(-\xi_2) + \text{Bi}^2(-\xi_2)\right]\,, \tag{2.34}$$

where

$$\xi_2 = \eta\left(\frac{4a\tau_{\alpha}}{\pi}\right)^{1/3}\,, \tag{2.35}$$

Ai and Bi represent the Airy function of first and second kind, respectively. See eq. (2.16) for a, τ_α and η. Similarly, I_i is the integral over the spectrum of injected photons given as [13]

$$I_i = \eta\sqrt{\frac{a\tau_\alpha}{2}} \int_0^\infty \left[\exp\left(-2\eta y - \frac{\pi y^3}{6a\tau_\alpha}\right) \mathrm{erfc}\left(\sqrt{\frac{\pi y^3}{2a\tau_\alpha}}\right) \frac{1}{\sqrt{y}}\right] \mathrm{d}y - \frac{\delta_\alpha(1-\delta_\alpha)}{2\eta} \,. \tag{2.36}$$

with δ_α given in eq. (2.14). The quantity J_α^i/J_α^c is decided by the stellar model. Here we take it to be 0.2.

Note that the free parameter introduced in section 2.1.3, f_α, directly affects q_α through $J_\alpha(z)$ which in turn is calculated from emissivity, eq. (2.19). This parameter has a small influence on the thermal history but a more dramatic effect on the 21-cm signal. See figure 1.

2.2.3 X-ray heating

Ultraviolet (UV) and X-ray photons from high-redshift galaxies ionize and heat the IGM. Due to the large cross-section of hydrogen atoms at UV wavelengths, the UV photons have short mean free path and are mainly responsible for ionizing the medium in close vicinity of the sources resulting in the so-called H II regions [112, 119, 120]. X-rays have very long mean free path, because of which they are able to penetrate far into the IGM. In the process, they heat and partially ionize the IGM [121]. The possible sources of X-rays include X-ray binaries [122, 123], inverse Compton scattering in supernova remnants [124] and mini-quasars [125]. X-ray binaries are a class of binary stars that are luminous in X-rays due to accretion from one of the stars onto another [126]. Evidence suggests that at high redshifts, such as those considered in this work, the dominant source could be high-mass X-ray binaries [127–129]. In canonical models of the 21-cm absorption feature at Cosmic Dawn, the Ly α photons create the absorption feature and X-ray photons destroy it.

X-ray heating is commonly characterised by three parameters, namely w, E_0 and f_X. These represent the power law index of the X-ray background spectral energy distribution (SED), the minimum energy of X-ray photons that can contribute to heating, and an overall normalisation of X-ray SED, respectively [27, 130]. In this work we keep w and E_0 fixed and vary only f_X. This is justified because the dependence of 21-cm signal on w is weak and E_0 is somewhat degenerate with f_X [131].

The observed relationship between the X-ray luminosity L_X and the star formation rate (SFR) in star-forming galaxies suggests a linear relationship [132, 133], which can be written as [134]

$$\frac{L_X}{\mathrm{SFR}} \approx 2.61 \times 10^{32}\,\mathrm{W}\,\left(\mathrm{M_\odot yr^{-1}}\right)^{-1} \,, \tag{2.37}$$

for photon energies 0.5–8 keV and a power law SED with $w \sim 1.5$. We extrapolate this relation over 0.2–30 keV assuming the same power law. The reason for extrapolating to lower energies is because of large cross-section of X-ray and neutral hydrogen interaction, which roughly goes as $\sigma(E) \propto E^{-3}$ but too low energy photons with $E < 0.2$ keV are excluded since they are absorbed into IGM over short distances from the source [16, 135]. Higher energy photons with $E > 30$ keV have longer mean free path but smaller cross section, which means they have a negligible contribution in heating. Thus, 0.2–30 keV seems to be a reasonable choice [136].

The SED (in units of number per unit energy per baryon) of X-rays is [17, 98],

$$\phi_X(E) = \frac{N_X}{E_0} \frac{w-1}{1-(E_0/E_1)^{w-1}} \left(\frac{E}{E_0}\right)^{-w-1} \,, \tag{2.38}$$

where $w = 1.5$ as already mentioned before, N_X is the number of X-ray photons emitted per stellar baryon, $E_0 = 0.2$ keV and $E_1 = 30$ keV are the minimum and maximum X-ray energy relevant for heating. We get $N_X \sim 1$ on extrapolating 0.5–8 keV L_X-SFR relation (given in eq. 2.37) to 0.2–30 keV.

In analogy with Ly α emissivity, we can now construct X-ray emissivity as follows (in units of number per unit time per unit energy per unit comoving volume) [17, 98]

$$\epsilon_X(E, z) = f_X \phi_X(E) \frac{\dot{\rho}_\star(z)}{m_b} \,, \tag{2.39}$$

where $m_{\rm b}$ is the average baryon mass (eq. 2.22) and $\dot\rho_\star$ is the comoving SFRD (eq. 2.23). We will vary $f_{\rm X}$ between 0.1 and 10, with 1 as its base model value. This choice is consistent with previous studies [19, 130]. In figure 1 we show how our gas temperature and 21-cm signal change when $f_{\rm X}$ is changed.

The microscopic mechanism of X-ray heating can be explained as follows [16, 21]. First, the X-rays photoionize the H I and He I. In this process hot energetic electrons are produced which dissipate their energy via atomic excitations, secondary ionizations, or collisions with other electrons. As a result the average kinetic energy, and hence the temperature of IGM, increases.

There are mainly two types of estimates for X-ray heating in literature. Some studies give this simply as a certain fraction of emissivity [16, 137, 138]. The other type is a more physically motivated version where it is calculated from the background specific intensity of X-rays, $J_{\rm X}$ [17, 98, 135]. We use the second version with the detailed mathematical structure as follows. The standard photoheating rate is [21]

$$H_{\rm X} = 4\pi \int_{E_0}^{E_1} (E - E_\infty)\sigma(E)J_{\rm X}(E,z)\,{\rm d}E\,, \tag{2.40}$$

where $E_\infty = 13.6\,{\rm eV}$ is the ionization energy of hydrogen, and $\sigma(E)$ is the photoionization cross-section of H I–X-ray interaction, which takes the following functional form [139]

$$\sigma(E) = 5.48 \times 10^{-18} \frac{(\mathcal{E}-1)^2}{(1+\sqrt{\mathcal{E}/32.88})^{2.96}} \mathcal{E}^{-4.02}\,{\rm m}^2\,, \tag{2.41}$$

for $\mathcal{E} = E/0.4298$ when E is expressed in eV. Because of the energy division explained in previous paragraph, the standard photoheating rates are reduced. The reduced rate can be written as $f_{\rm X,h}H_{\rm X}$, where the reduction factor is given by [140]

$$f_{\rm X,h} = 1 - \left(1 - x_{\rm e}^{0.2663}\right)^{1.3163}\,. \tag{2.42}$$

The final term to be inserted in eq. (2.31) is

$$\frac{2q_{\rm X}}{3n_{\rm b}k_{\rm B}H} = \frac{8\pi}{3}\frac{1-x_{\rm e}}{1+x_{\rm He}+x_{\rm e}}\frac{f_{\rm X,h}}{k_{\rm B}H}\int_{E_0}^{E_1}(E-E_\infty)\sigma(E)J_{\rm X}(E,z)\,{\rm d}E\,. \tag{2.43}$$

The background specific intensity of X-rays is $J_{\rm X}$, analogous to J_α. We define it in terms of number per unit time per unit energy per unit area per unit solid angle. It can be calculated from the comoving X-ray emissivity of the source $\epsilon_{\rm X}$ (eq. 2.39) as

$$J_{\rm X}(E,z) = \frac{c(1+z)^2}{4\pi}\int_z^{z_\star}\frac{\epsilon_{\rm X}(E',z')}{H(z')}e^{-\tau_{\rm X}(E,z,z')}{\rm d}z'\,, \tag{2.44}$$

where $z_\star \sim 60$ is the redshift when the star formation starts [136], and $E' = E(1+z')/(1+z)$.

The X-ray optical depth can be written as

$$\tau_{\rm X}(E,z,z') = \int_z^{z'}\frac{c\,{\rm d}z''}{(1+z'')H(z'')\lambda_{\rm X}(E'',z'')}\,, \tag{2.45}$$

where $E'' = E(1+z'')/(1+z)$ and X-ray mean free path is approximately [92]

$$\lambda_{\rm X}(E,z) = \frac{1.1\bar{x}_{\rm HI}^{-1/3}}{(1+z)^3}\left(\frac{E}{300\,{\rm eV}}\right)^3\,{\rm Gpc}\,, \tag{2.46}$$

in proper units. A better version of $\lambda_{\rm X}$ would be written in terms of a sum over number density and photoionization cross section for all species involved, such as the one in ref. [98]. But here we will continue to use the approximation in eq. (2.46).

Note that the atomic excitations by the electrons released in photoionization can also generate Ly α photons. This is modelled simply by saying that this extra Ly α emissivity is a fraction of the X-ray emissivity. In this work, however, we have neglected that contribution (see for e.g. [141]).

2.3 Electron fraction and ionization rates

The photons and electrons from Hawking emission also cause ionization of IGM by a mechanism similar to the X-ray photons and secondary ionization by electrons. The differential equation relevant for our work governing the evolution of electron fraction in the IGM is [21, 84]

$$(1+z)H\frac{\mathrm{d}x_\mathrm{e}}{\mathrm{d}z} = \alpha(T_\mathrm{k})n_\mathrm{H}x_\mathrm{e}^2 - \Gamma_\mathrm{X}(1-x_\mathrm{e}) - \Gamma_\mathrm{HR}\,, \tag{2.47}$$

where the first term on the right hand side is recombination term and the two negative terms are the ionization terms due to the X-ray background and Hawking radiation from PBHs. An approximate temperature dependence of recombination coefficient can be expressed as [142]

$$\alpha(T) = 2.5 \times 10^{-16}\frac{T^{-0.7}}{1 + \left[T/(10^6\,\mathrm{K})\right]^{0.7}}\,\mathrm{m}^3\mathrm{s}^{-1}\,, \tag{2.48}$$

with T being in K.

The standard photoionization rate due to X-rays is given by

$$\Gamma_\mathrm{X}(z) = 4\pi\int_{E_0}^{E_1}\sigma(E)J_\mathrm{X}(E,z)\,\mathrm{d}E\,, \tag{2.49}$$

but it gets slightly enhanced due to secondary ionizations [21]. Thus, we make the following replacement

$$\Gamma_\mathrm{X} \to \Gamma_\mathrm{X} + \frac{f_\mathrm{X,ion}}{E_\infty}H_\mathrm{X}\,, \tag{2.50}$$

where H_X was defined in eq. (2.40). The enhancement factor is [140]

$$f_\mathrm{X,ion} = 0.3908\left(1 - x_\mathrm{e}^{0.4092}\right)^{1.7592}\,. \tag{2.51}$$

For higher accuracy the factors $f_\mathrm{X,h}$ and $f_\mathrm{X,ion}$ may be used from ref. [143], but we will continue with the ones from ref. [140].

We defer a discussion on ionization due to HR, i.e., Γ_HR, in section 3.

2.4 Excess radio background

We have so far considered only the standard astrophysics. However, as mentioned in section 1, we need extra physical input in order to match the EDGES signal. We assume that there exists a uniform excess radio background in the sky. For radio frequencies the usual approximation of Rayleigh-Jeans limit works very well which allows us to quantify the energy flux in terms of a 'temperature'. This radio flux is fit very well by a power law as observed by ARCADE 2 and LWA1 [28, 29]. The combined CMB temperature and excess radio measured today at frequency ν can be written as

$$T_\mathrm{r}(\nu) = T_0 + T_\mathrm{R}\left(\frac{\nu}{\nu_0}\right)^\beta\,, \tag{2.52}$$

where $T_0 = 2.725\,\mathrm{K}$ is the CMB temperature measured today, $T_\mathrm{R} = 24.1\,\mathrm{K}$, $\beta \approx -2.6$ [29] and reference frequency $\nu_0 = 310\,\mathrm{MHz}$. Generalising the above for an earlier epoch at redshift z and measurement made for the frequency corresponding to 21-cm line (redshifted to z, i.e. $\nu = \nu_\mathrm{21cm}/(1+z)$) we get [26, 27]

$$T_\mathrm{r}(z) = 2.725(1+z)\left[1 + 0.169\,\zeta_\mathrm{ERB}(1+z)^{2.6}\right]\,, \tag{2.53}$$

where we have parametrized the amplitude of excess radio — the coefficient of the second term on the right hand side of eq. (2.52) — by ζ_ERB. We vary ζ_ERB between 0.01 and 1 with $\zeta_\mathrm{ERB} = 1$ as the base value corresponding to the excess observed by ARCADE 2. As with other parameters figure 1 justifies the choice of this range.

Note that refs. [144, 145] considered an enhancement in the background, against which we measure our 21-cm brightness, due to the radiation emitted by accreting black holes of intermediate or supermassive black holes. However, ultralight PBHs in the mass range 10^{15}–10^{17} g cannot produce photons of wavelength 21 cm either via accretion or via evaporation.[3]

3 Hawking radiation from primordial black holes

Primordial black holes emit particles via Hawking radiation and the spectrum of the emitted particles follows a blackbody like distribution. The emission rate of particles from a neutral and non-rotating PBH of temperature T_{PBH}, in the energy interval E and $E + \mathrm{d}E$ is given by [147–152]

$$\mathrm{d}\dot{N} = \frac{1}{2\pi\hbar} \frac{\Gamma_s(E, \mu, T_{\mathrm{PBH}})}{\exp\left(\frac{E}{k_{\mathrm{B}}T_{\mathrm{PBH}}}\right) - (-1)^{2s}} \mathrm{d}E , \qquad (3.1)$$

where $\hbar = h_{\mathrm{P}}/2\pi$ is the reduced Planck's constant, s denotes the spin of the emitted particle and Γ_s denotes a dimensionless absorption coefficient, commonly known as the greybody factor. For a neutral, and non-rotating PBH, the greybody factor depends on the energy of the emitted particle E, temperature of the PBH T_{PBH}, spin of the emitted particle s, and the rest mass of the emitted particle μ. In the high energy limit ($G_{\mathrm{N}}M_{\mathrm{PBH}}E/\hbar c^3 \gg 1$), the greybody factor becomes independent of the spin of the emitted particle and reaches its geometrical saturation value, i.e. $\Gamma = 27\, G_{\mathrm{N}}^2 E^2 (M_{\mathrm{PBH}}^2 - \mu^2)/\hbar^2 c^6$. Whereas, in the opposite regime ($G_{\mathrm{N}}M_{\mathrm{PBH}}E/\hbar c^3 \ll 1$), it has a very strong dependence on the spin of the emitted particles [150, 152].

The temperature of an uncharged, non-rotating PBH is solely determined by its mass M_{PBH} [147–152]

$$k_{\mathrm{B}}T_{\mathrm{PBH}} = \frac{\hbar c^3}{8\pi G_{\mathrm{N}} M_{\mathrm{PBH}}} = 1.06 \left(\frac{10^{13}\,\mathrm{g}}{M_{\mathrm{PBH}}}\right) \mathrm{GeV} . \qquad (3.2)$$

As the energy of the emitted particles becomes comparable to the temperature of a PBH, i.e. $E \sim k_{\mathrm{B}}T_{\mathrm{PBH}}$, significant Hawking emission occurs. Quantitatively, Hawking emission peaks at $E_{\mathrm{peak}} = 2.81\, k_{\mathrm{B}}T_{\mathrm{PBH}}$ for $s = 0$ particle species, $E_{\mathrm{peak}} = 4.02\, k_{\mathrm{B}}T_{\mathrm{PBH}}$ for $s = 1/2$ particle species, and $E_{\mathrm{peak}} = 5.77\, k_{\mathrm{B}}T_{\mathrm{PBH}}$ for $s = 1$ particle species [152]. Note that, for energies exceeding the peak value ($E \gg E_{\mathrm{peak}}$), Hawking emission is exponentially suppressed, and for energies lower than the peak value ($E \ll E_{\mathrm{peak}}$), it falls off as a power law.

For this work, we calculate the spectrum of the emitted particles, $\mathrm{d}\dot{N}/\mathrm{d}E$, using the publicly available code `BlackHawk`[4] [153]. We have verified the numerically obtained Hawking emission rates against the semi-analytical emission rates from refs. [148, 149].

Hawking-radiated particles (photons γ, electrons e^-, positrons e^+) interact with the ordinary baryonic matter in the IGM and deposit energy. The energy deposition typically occurs through five different channels which include hydrogen ionization, helium ionization, hydrogen excitation, IGM heating and sub-10.2 eV continuum photons [154, 155]. However, for this work, only hydrogen ionization and IGM heating are relevant because we are ignoring the helium recombination-ionization [98], hydrogen excitation is also irrelevant for reasons discussed later and sub-10.2 eV continuum photons are involved in CMB spectral distortions, which is again not important for our work [156]. The power density (energy per unit time per unit volume) going into a particular channel 'c' is

$$q_{\mathrm{HR,c}} = \iint \left[f_{\mathrm{c}}(E_\gamma, z) E_\gamma \left(\frac{\mathrm{d}\dot{N}}{\mathrm{d}E}\right)_\gamma + 2 f_{\mathrm{c}}(E_{\mathrm{e}} - m_{\mathrm{e}}c^2, z)(E_{\mathrm{e}} - m_{\mathrm{e}}c^2) \left(\frac{\mathrm{d}\dot{N}}{\mathrm{d}E}\right)_{\mathrm{e}^\pm} \right]$$
$$\times\, n_{\mathrm{PBH}}(M_{\mathrm{PBH}}) \psi(M_{\mathrm{PBH}})\, \mathrm{d}M_{\mathrm{PBH}}\, \mathrm{d}E , \quad (3.3)$$

---

[3]We find the brightness temperature at a photon energy of 5.9 μeV corresponding to the primary spectrum from a 10^{17} g PBH to be $\sim 10^{-46}$ K. However, we have not explored the same for secondary spectrum which may or may not contribute [146].

[4]https://blackhawk.hepforge.org/

where E is the total energy of the emitted particle, n_{PBH} is the number density of PBHs, $\psi(M_{\mathrm{PBH}})$ denotes the probability distribution function of PBH masses, and $f_{\mathrm{c}}(E_{\mathrm{K}}, z)$ denotes the ratio of the energy deposited into channel c to the injected energy as a function of kinetic energy of the emitted particle E_{K} and redshift z. We use the numerical data table of f_{c} corresponding to DM decay from ref. [154] which are in close agreement with that of ref. [155].

In this work, we consider a monochromatic mass distribution of PBHs, for which $\psi(M_{\mathrm{PBH}})$ is a Dirac delta function centred at M_{PBH}. Equation (3.3) then simplifies to

$$q_{\mathrm{HR,c}} = \int \left[f_{\mathrm{c}}(E_{\gamma}, z) E_{\gamma} \left(\frac{\mathrm{d}\dot{N}}{\mathrm{d}E} \right)_{\gamma} + 2 f_{\mathrm{c}}(E_{\mathrm{e}} - m_{\mathrm{e}}c^2, z)(E_{\mathrm{e}} - m_{\mathrm{e}}c^2) \left(\frac{\mathrm{d}\dot{N}}{\mathrm{d}E} \right)_{\mathrm{e}^{\pm}} \right]$$
$$\times\, n_{\mathrm{PBH}}(M_{\mathrm{PBH}})\mathrm{d}E \,. \quad (3.4)$$

Since PBHs make up the solitary component of the present day DM, the number density of PBHs can be written as

$$n_{\mathrm{PBH}} = f_{\mathrm{PBH}} \frac{\rho_{\mathrm{c}} \Omega_{\mathrm{DM}}}{M_{\mathrm{PBH}}} \,, \quad (3.5)$$

where f_{PBH} denotes the fraction of DM composed of PBHs, ρ_{c} is the critical density of the Universe, and Ω_{DM} denotes the present day DM density relative to ρ_{c}. Note that, $q_{\mathrm{HR,c}}$ is almost independent of the redshift because for $M_{\mathrm{PBH}} \geqslant 10^{15}$ g, the mass loss of PBHs due to Hawking emission is negligible and f_{c} has a weak dependence on z for the range considered in this work.

Using eq. (2.31), the heating term now is

$$\frac{2 q_{\mathrm{HR,heat}}}{3 n_{\mathrm{b}} k_{\mathrm{B}} H} = f_{\mathrm{PBH}} \frac{2 m_{\mathrm{b}}}{3 k_{\mathrm{B}} H} \left(\frac{\Omega_{\mathrm{m}}}{\Omega_{\mathrm{b}}} - 1 \right) \frac{1}{M_{\mathrm{PBH}}}$$
$$\times \int \left[f_{\mathrm{heat}}(E_{\gamma}, z) E_{\gamma} \left(\frac{\mathrm{d}\dot{N}}{\mathrm{d}E} \right)_{\gamma} + 2 f_{\mathrm{heat}}(E_{\mathrm{e}} - m_{\mathrm{e}}c^2, z)(E_{\mathrm{e}} - m_{\mathrm{e}}c^2) \left(\frac{\mathrm{d}\dot{N}}{\mathrm{d}E} \right)_{\mathrm{e}^{\pm}} \right] \mathrm{d}E \,, \quad (3.6)$$

where average baryon mass, m_{b}, is given by eq. (2.22). Similarly, the ionization rate due to Hawking emission from the ground state of hydrogen atom, required in eq. (2.47), can be written as

$$\Gamma_{\mathrm{HR}} = \frac{q_{\mathrm{HR,ion}}}{n_{\mathrm{H}} E_{\infty}} \,, \quad (3.7)$$

where $E_{\infty} = 13.6\,\mathrm{eV}$ is the ionization energy of hydrogen. In figure 1 we show the effect on the 21-cm signal when f_{PBH} is varied for a PBH of mass $M_{\mathrm{PBH}} = 10^{15}$ g.

The difference between our standard equation of thermal evolution, eq. (2.31), and eq. (11) from previous analysis [84] is mainly in accounting of different astrophysical processes. Other than the adiabatic cooling and Compton heating we also consider Ly α and X-ray heating. On comparing our ionization equations, eq. (2.47), and eq. (3) from ref. [84] we find the following differences. Firstly, we identify that the collisional ionization is negligible for the epoch of our interest and hence the term with coefficient β can be ignored. Secondly, unlike previous literature we incorporate X-ray photons which, other than heating, are also involved in the ionization of IGM. Thirdly, we do not have the Peebles C factor, which can be interpreted as the probability for an atom initially in the first excited state to reach the ground state before being ionized. For redshifts considered in this work, it can be set to 1 to an excellent approximation [157, 158]. Lastly, because $C = 1$, we can say that the ionizations from the first excited state are negligible. This explains our exclusion of the term $I_{\mathrm{X}_{\alpha}}(z)$ seen in ref. [84].

Specific to 21-cm calculation, while ref. [84] used the data from ref. [159] to calculate Ly α coupling, we have taken a more physically motivated approach for this as highlighted in section 2.1. Finally, we comment on the differences in PBH modelling. Previous literature (e.g. refs. [84, 87]) have used the following to estimate the mass loss rate due to Hawking radiation

$$\frac{\mathrm{d}M_{\mathrm{PBH}}}{\mathrm{d}t} = -5.34 \times 10^{25} \mathcal{F}(M_{\mathrm{PBH}}) \left(\frac{1\,\mathrm{g}}{M_{\mathrm{PBH}}} \right)^2 \mathrm{g\,s^{-1}} \,, \quad (3.8)$$

where $\mathcal{F}(M_{\mathrm{PBH}})$ is a measure of the number of emitted particle species, normalised to unity for a black hole of mass $M_{\mathrm{PBH}} \gg 10^{17}\,\mathrm{g}$ [151]. Then using the expression of $\dot{M}_{\mathrm{PBH}}$, the rate of energy injection per unit volume was given as $q_{\mathrm{inj}} = -n_{\mathrm{PBH}}\dot{M}_{\mathrm{PBH}}c^2$.

4 Inference procedure

We now explain the inference procedure that we use to constrain our model parameters from the EDGES data.[5] We follow a Bayesian procedure with a Gaussian likelihood. Our approach is similar to ref. [138]. We emphasise that we use the full information content of the EDGES data by using their measurements at all of 123 redshift points, rather than focusing on some specific features of the signal [130, 138].

Let $\Delta T_{\mathrm{b}}^{\mathrm{exp}} = \Delta T_{\mathrm{b}}^{\mathrm{exp}}(z)$ and $\Delta T_{\mathrm{b}}^{\mathrm{theo}} = \Delta T_{\mathrm{b}}^{\mathrm{theo}}(\theta, z)$ represent the data and the model values, respectively, of the 21-cm signal at redshift z and θ being the set of n parameters that parametrize our model. Our likelihood is then

$$\mathcal{L}(\Delta T_{\mathrm{b}}^{\mathrm{exp}}|\theta) = \prod_{i=1}^{123} \frac{1}{\sqrt{2\pi}\varepsilon_i} \exp\left[-\frac{\left(\Delta T_{\mathrm{b}}^{\mathrm{exp}} - \Delta T_{\mathrm{b}}^{\mathrm{theo}}\right)_i^2}{2\varepsilon_i^2} \right] , \qquad (4.1)$$

where ε_i are the $1\,\sigma$ uncertainties in the data for the redshift bin i. The label i in the above equation runs over the 123 data points corresponding to the different redshift bins. We have suppressed θ and z dependence on the right hand side for simplicity.

We take a constant uncertainty for all the redshift bins, i.e., $\varepsilon_i = 0.05\,\mathrm{K}$. Some remarks are in order about this. In the result presented by the EDGES collaboration, i.e., in Bowman et al. (2018) [7], only the uncertainty on the amplitude of the absorption at a particular redshift of $z \approx 17$ is presented. This uncertainty estimate is not useful if one intends to infer constraints using the full frequency range of the EDGES data. This problem has been noted before, and in response other groups have inferred uncertainties for the entire frequency range of the EDGES data. For example, Hills et al. (2018) [160] provide an uncertainty estimate of $0.025\,\mathrm{K}$ at all frequencies within the EDGES band. See, e.g., Chatterjee et al. (2021) [161], who use a frequency-independent $0.025\,\mathrm{K}$ uncertainty, or Mirocha & Furlanetto (2019) [136], who assumed a frequency-independent $0.1\,\mathrm{K}$ uncertainty throughout the EDGES band. Since an important motivation in our work is to use the information from the full EDGES band, we follow the same approach, albeit with a slightly more conservative estimate for the uncertainty of $0.05\,\mathrm{K}$. Choosing $0.025\,\mathrm{K}$ will not change any of our constraints, except to slow down the MCMC convergence. As we will see below, our constraints on f_{PBH} are significantly stronger than other constraints published in the literature. We stress that this strength is because we have used information from the full EDGES band. Consequently, our inference stays fairly robust against changes to the uncertainty estimates on the EDGES data points. The constraint does not critically depend on the uncertainty on the EDGES absorption profile, but rather on its shape.

We choose uniform priors on our model parameters in the ranges tabulated in table 1. This choice of our priors covers a large range of values around the EDGES data, as shown in figure 1. Note that the prior on $\log_{10} f_{\mathrm{PBH}}$ changes with PBH mass. For example, in the presence of X-ray heating the prior required for a PBH of mass $10^{15}\,\mathrm{g}$ is $[-11.0, -9.0]$, while that for a PBH of mass $10^{16}\,\mathrm{g}$ is $[-6.5, -3.0]$. This choice of a mass-dependent prior might appear odd, but it merely reflects the fact that large values of $\log_{10} f_{\mathrm{PBH}}$ are obviously ruled out due to the enormous heating rates. One could in principle choose a wide prior, such as $[-11, 0]$, for all masses. But this would waste considerable computational effort. For instance, for a $10^{15}\,\mathrm{g}$ black hole, the best-fit f_{PBH} is $\sim 10^{-9}$, so exploring f_{PBH} up to 1 for this mass would imply heating rate higher by nine orders of magnitude which is clearly ruled out by the EDGES observation.

---

[5]http://loco.lab.asu.edu/edges/edges-data-release/

Parameter	Description	Min	Max
$\log_{10} f_\alpha$	Controls the strength of Ly α background, eq. (2.19)	-2	2
$\log_{10} T_{\mathrm{vir},4}$	Minimum virial temperature of dark matter haloes, eq. (2.26)	-0.75	1.25
$\log_{10} f_{\mathrm{X}}$	Controls the strength of X-ray background, eq. (2.39)	-1	1
$\log_{10} \zeta_{\mathrm{ERB}}$	Controls the strength of excess radio, eq. (2.53)	-2	0
$\log_{10} f_{\mathrm{PBH}}$	Fraction of DM in the form of PBHs, eq. (3.5)	$-$	$-$

Table 1: Model parameters used in this work, with the ranges of values over which uniform prior PDFs are used. The range of values for $\log_{10} f_{\mathrm{PBH}}$ depends on the mass of PBH under consideration (see text).
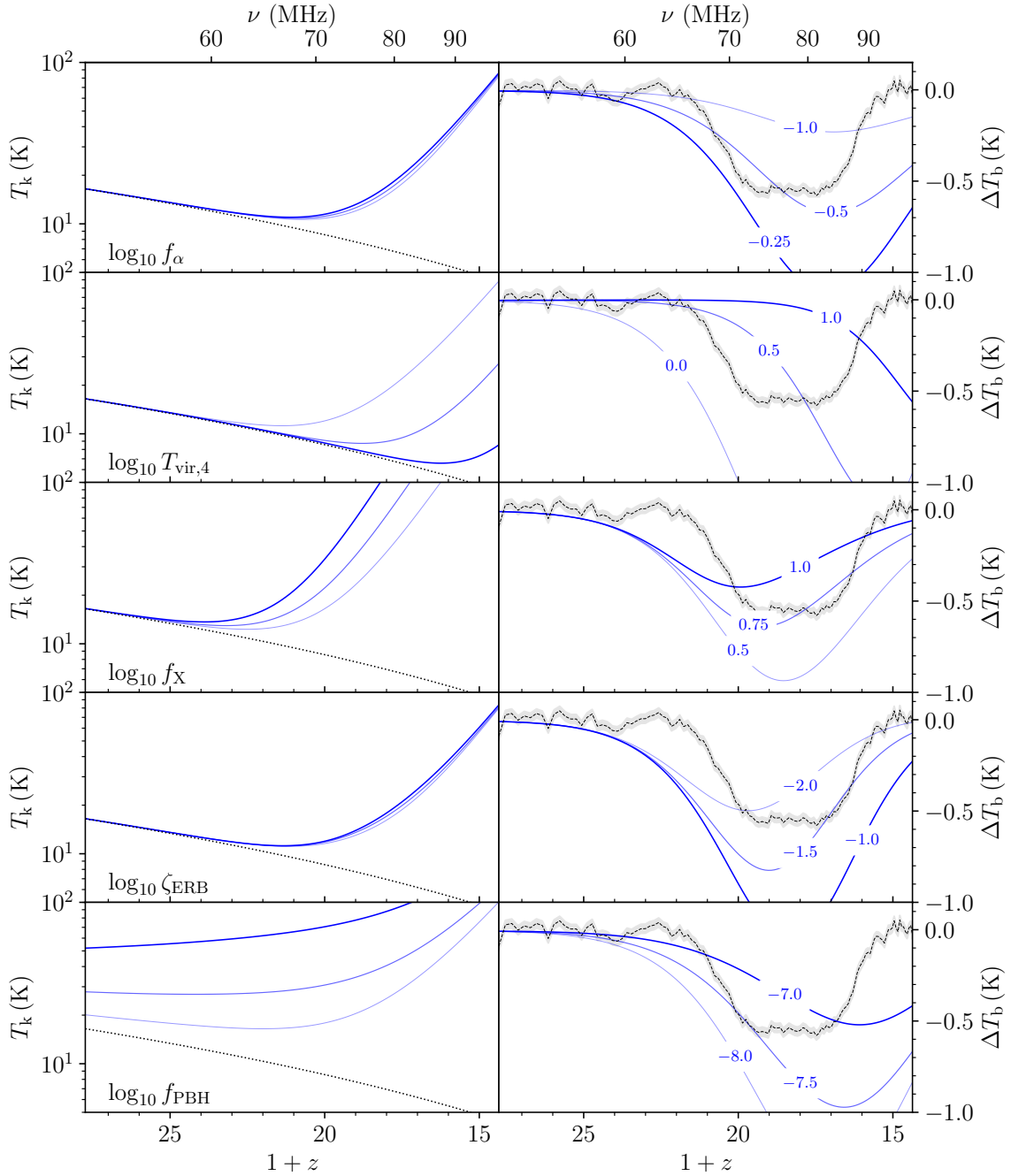
Figure 1: Gas temperature evolution (left column) and the corresponding 21-cm signal (right column) for a range of parameter values. For reference, we show the adiabatic thermal evolution in all panels of the left column, and the EDGES measurement of the 21-cm signal in all panels of the right column. In each row, a single parameter is varied, while the remaining parameters are held fixed at 0, unless one of these fixed parameters is $\log_{10} f_{\rm PBH}$. When $\log_{10} f_{\rm PBH}$ is held fixed, it is assigned a value of -10, and a PBH mass of 10^{15} g is assumed. Because PBH-induced heating has a broadband effect on the signal, even the falling edge of the 21-cm absorption signal can constrain the PBH fraction. See text for a discussion.

We now present a pedagogical discussion of figure 1:

(a) Ly α photons affect the 21-cm signal via two effects: heating and coupling. A higher value of f_α implies a stronger background which in turn means more heating but also a stronger coupling. Heating has a reducing effect on the absorption feature while stronger coupling produces a deeper absorption feature. On the whole the latter wins since Ly α heating is not a very efficient heating mechanism [13] as evident from 1$^{\text{st}}$ panel.

(b) When the minimum virial temperature is smaller, more star forming haloes are allowed and thus more SFRD. This results in a stronger Ly α coupling resulting in a deeper 21-cm signal. But the more important role of this parameter is to change the timing of the first drop in the signal without affecting the shape.

(c) As f_X takes higher values, the X-ray background gets stronger which implies more X-ray heating. This in turn raises T_k, and hence T_s, thus reducing ΔT_b.

(d) When we increase ζ_{ERB} we allow more excess radio background and hence a stronger contrast between the 21-cm brightness and the background, thus producing a deeper absorption signal.

(e) Higher f_{PBH} imply more number of PBHs and hence more heating, which in turn reduces the 21-cm signal. The PBH considered for these plots is of mass 10^{15} g.

With likelihood and priors ready, we can use the Bayes theorem to construct the posterior distribution as

$$P(\theta|\Delta T_b^{\text{exp}}) \propto \mathcal{L}(\Delta T_b^{\text{exp}}|\theta)\mathcal{P}(\theta)\,, \tag{4.2}$$

where $\mathcal{P}(\theta)$ represents the prior distribution. Since we will use a MCMC implementation [162] for sampling $P(\theta|\Delta T_b^{\text{exp}})$, the normalisation of the above is unnecessary. To explore the nD parameter space we use the publicly available code emcee[6] [163]. We run 64 Markov chains (number of 'walkers') and 5000 steps for each parameter, which is a reasonable length since the autocorrelation time for any parameter is not more than ~ 50. We obtain the initial guess for parameters by maximising $\mathcal{L}(\Delta T_b^{\text{exp}}|\theta)$ when treated as a function of θ. The thermalisation time (number of burn-in steps) is less than 100. Once we have obtained the parameter set, θ_{BF}, which best explain the model we test the goodness-of-fit by the reduced chi-squared statistics given by χ^2/dof. The standard definition of χ^2 is given by

$$\chi^2 = \sum_{i=1}^{123} \frac{\left[\Delta T_b^{\text{exp}}(z_i) - \Delta T_b^{\text{theo}}(\theta_{\text{BF}}, z_i)\right]^2}{\varepsilon_i^2}\,, \tag{4.3}$$

and 'dof' stands for degrees of freedom. It is equal to the number of data points minus the number of free parameters employed in the model.

Note that calculating ΔT_b^{theo} for any set of parameters during an MCMC simulation can be time consuming and expensive. To overcome this difficulty we prepare our ΔT_b^{theo} at some specific grid points in the nD space of parameters before running MCMC sampler. With these pre-calculated ΔT_b^{theo}s we can then estimate ΔT_b^{theo} at the desired intermediate parameter set using multi-dimensional linear interpolation. If we have p number of evenly spaced points in each of the n dimensions then we have a total of p^n number of models.

As the X-ray emissivity at Cosmic Dawn is unknown, it is interesting to consider PBHs as the sole heating mechanism that terminates the 21-cm absorption signal. We therefore consider two distinct scenarios for our inference: one without X-ray heating and the other with X-ray heating. In the following subsections we give the details of our analysis for these two cases. The aim in both cases is the same: to obtain the allowed values of the fraction of DM in the form of PBHs, i.e., f_{PBH} as a function of PBH mass.

---

[6]https://github.com/dfm/emcee.

Case I: analysis assuming X-ray heating is absent

In the absence of X-ray heating, the four major physics components affecting the 21-cm signal are SFRD, Ly α coupling, HR heating and ERB. The degrees of freedom, dof, is $123 - 4 = 119$. Our model parameters in this case are

$$\theta = \{\log_{10} f_\alpha, \ \log_{10} T_{\mathrm{vir},4}, \ \log_{10} \zeta_{\mathrm{ERB}}, \ \log_{10} f_{\mathrm{PBH}}\}. \tag{4.4}$$

We choose $p = 9$ points for each of these parameters, so that we have a total of $9^4 = 6561$ models explored. However, note that an MCMC simulation with all the parameters varying is not required for each mass. We need to run the 4-parameter MCMC for just one mass, say $M_{\mathrm{PBH}} = 10^{15}$ g, to obtain the best-fitting parameters. Once this is done, we can fix all parameters other than f_{PBH}, i.e., $T_{\mathrm{vir}}, f_\alpha$ and ζ_{ERB} to their best-fitting values so that for the remaining masses we have only one parameter to vary. We do the analysis for the following PBH masses

$$10^{15}, 2 \times 10^{15}, 3 \times 10^{15}, \ldots 7 \times 10^{16} \, \mathrm{g},$$

which make a total of 16 masses. The reason for this preferred method of analysis is explained as follows. The Hawking emission, $q_{\mathrm{HR,c}}$, has nearly the same trend as a function of time (a constant throughout the epoch of our interest for a given mass) for all masses. Stated differently, $q_{\mathrm{HR,c}}$ for different masses differ by a constant factor (see also the discussion in section 6). Because our parameter is $\log_{10} f_{\mathrm{PBH}}$ rather than f_{PBH}, the above reasoning implies that the probability distribution of $\log_{10} f_{\mathrm{PBH}}$ and its covariances with other parameters will just shift by a certain amount for different masses.

Case II: analysis allowing for X-ray heating

Four out of five physics components are same as before, but now we have X-ray heating as well. The degrees of freedom, dof, is $123 - 5 = 118$. The models parameters are

$$\theta = \{\log_{10} f_\alpha, \ \log_{10} T_{\mathrm{vir},4}, \ \log_{10} f_{\mathrm{X}}, \ \log_{10} \zeta_{\mathrm{ERB}}, \ \log_{10} f_{\mathrm{PBH}}\}. \tag{4.5}$$

We choose $p = 5$ points for each of these parameters, so that we have a total of $5^5 = 3125$ models explored. Just as with case I we need not run the 5-parameter MCMC simulation for all masses. Once we have obtained the non-PBH best-fitting parameter values we can set all of them to these, except f_{PBH}, for the remaining masses. We do the analysis for the following PBH masses

$$10^{15}, 2 \times 10^{15}, 3 \times 10^{15}, \ldots 3 \times 10^{17} \, \mathrm{g},$$

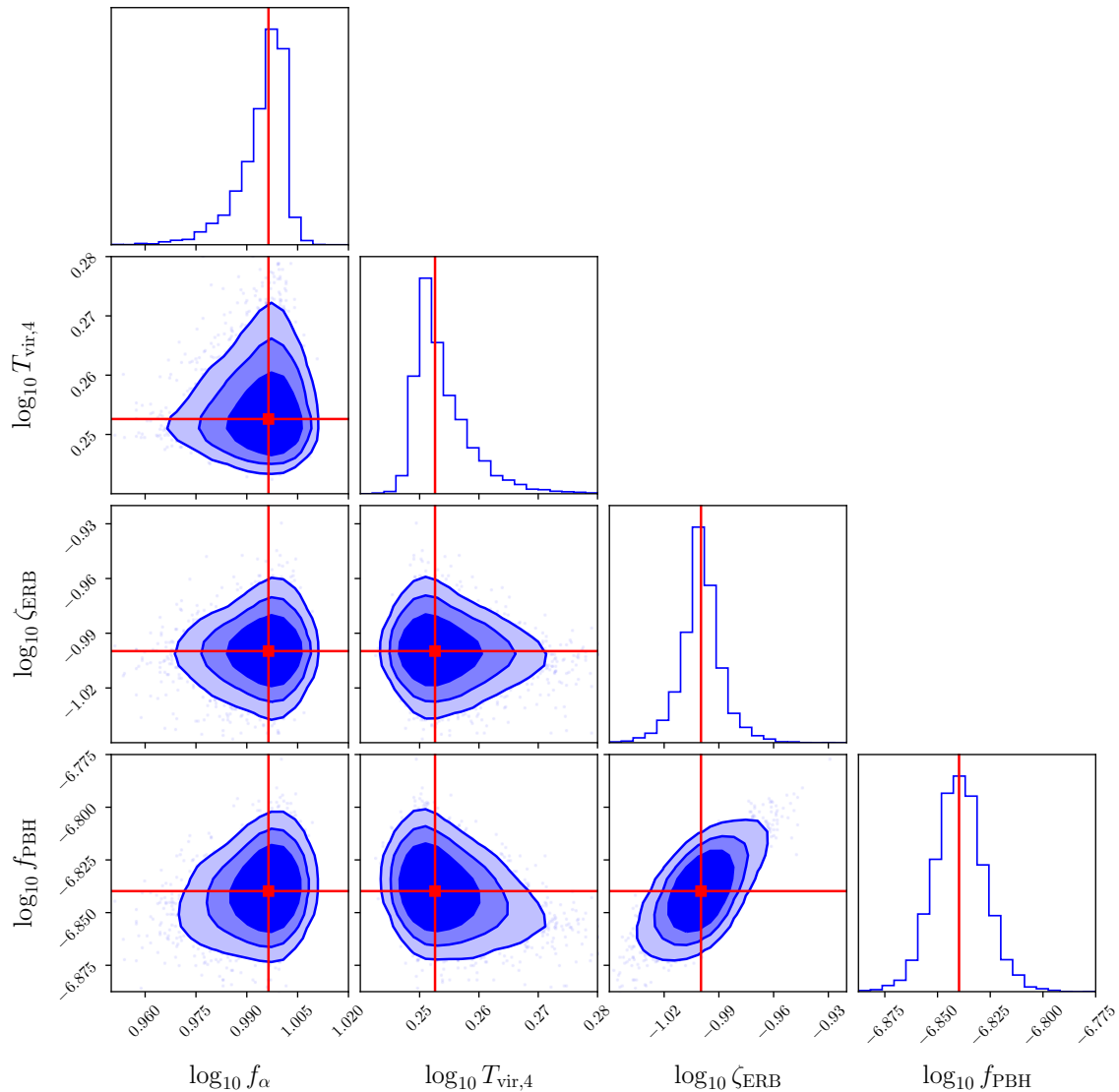which make a total of 21 masses.

Note a very fundamental difference between the two analysis. In case II we will only obtain an upper bound on f_{PBH}. But case I produces a detection of PBHs as in this scenario there are no alternative heating sources that can result in the low-redshift rising edge of the 21-cm absorption profile. Case II is arguably more conservative as some X-ray emission is perhaps easily plausible at these redshifts (see discussion in section 2.2) but until such high-redshift X-ray sources are known to exist, case I remains a valid possibility. We discuss this further below.

5 Results

### 5.1 Constraints by assuming X-ray heating to be absent

Our marginalised two-dimensional and one-dimensional posterior distributions in the case without X-ray heating are shown in figure 2. The best-fitting parameter values with 90% confidence intervals, when we use a PBH of mass $M_{\mathrm{PBH}} = 10^{15}$ g, are

$$\log_{10} f_\alpha = 0.9964^{+0.0057}_{-0.0164},$$
$$\log_{10} T_{\mathrm{vir},4} = 0.2526^{+0.0111}_{-0.0039},$$
$$\log_{10} \zeta_{\mathrm{ERB}} = -0.9998^{+0.0189}_{-0.0187},$$
$$\log_{10} f_{\mathrm{PBH}} = -6.8398^{+0.0199}_{-0.0192}.$$

Figure 2: Two-dimensional and one-dimensional marginalised posterior probability distributions of parameters for a PBH of mass $M_{\mathrm{PBH}} = 10^{15}\,\mathrm{g}$ in a model with no X-ray heating. The contour lines show the 68.3%, 86.6% and 95.5% levels corresponding to 1-sigma, 1.5-sigma and 2-sigma, respectively. The red lines show the median values.

The best-fitting 21-cm signal, 90% confidence interval and its comparison with the EDGES signal are shown in figure 3 for PBHs of mass $10^{15}\,\mathrm{g}$. Using the definition of goodness-of-fit given in eq. (4.3) we get $\chi^2/\mathrm{dof} = 910.5/119$. For discussion we can divide the complete range into three regions: A, B and C which are the regions on the left of the absorption, the absorption itself and the right side of the absorption, respectively. We see that there is some residual gap in best-fitting curve and data in all A, B and C. Other parameters being fixed, decreasing f_{PBH} may give the correct absorption depth but will increase the errors in regions A and C. On the other hand if we increase f_{PBH} we get better fits in A and C but with increased error in B. Thus, we see that there is an optimum value of f_{PBH} with best fits the signal given some uncertainty ε. A similar reasoning applies for other parameters as well.
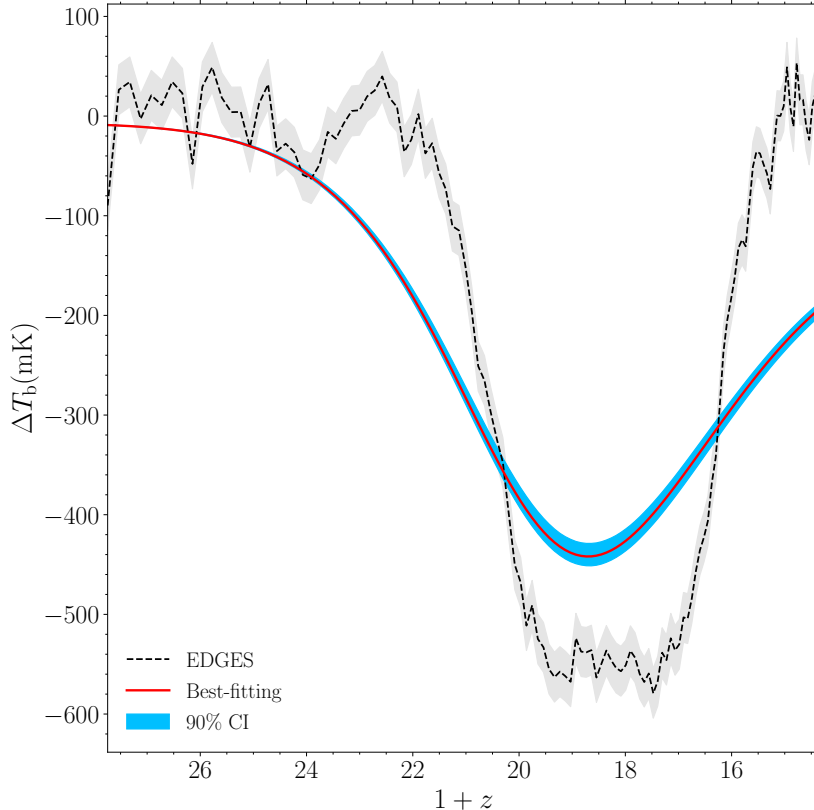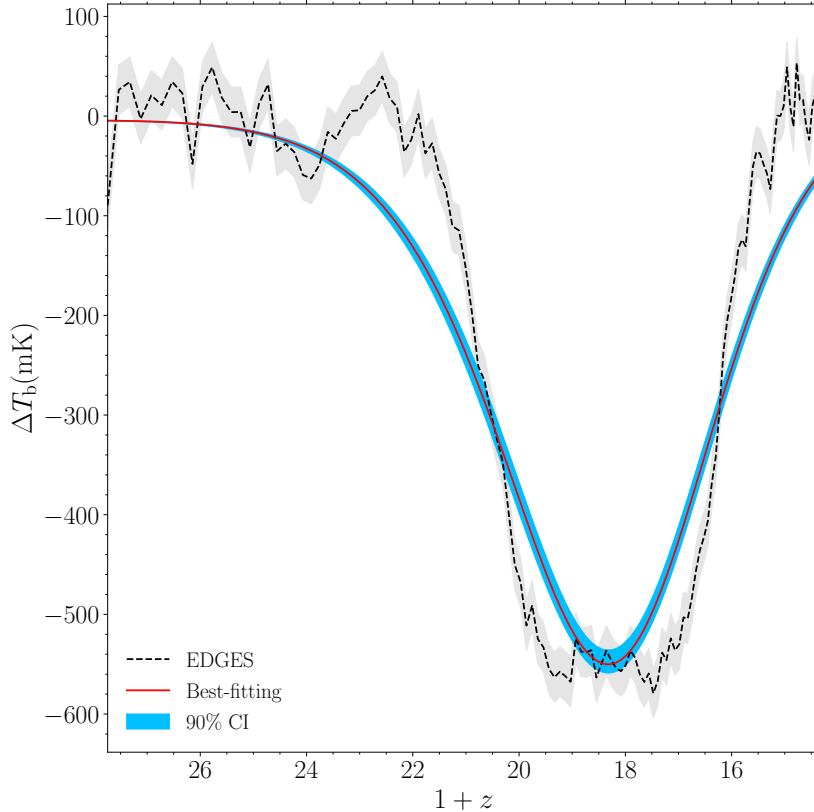
Figure 3: Red curve shows the derived posterior median 21-cm signal in the absence of an X-ray background. The blue shaded region shows the 90% confidence intervals (CI). This is for PBH of mass 10^{15} g, and corresponds to $\log_{10} f_{\mathrm{PBH}} = -6.8398^{+0.0199}_{-0.0192}$. The EDGES measurement is shown by the black dashed curve, with the grey shaded region around it showing the uncertainty. The goodness-of-fit is $\chi^2/\mathrm{dof} = 910.5/119$.

5.2 Constraints allowing for X-ray heating

We now discuss the second case in which we would like to find bounds on f_{PBH} when there is X-ray heating. The best-fitting non-PBH parameter values obtained are

$$\log_{10} f_\alpha = 0.0207^{+0.0073}_{-0.0071},$$
$$\log_{10} T_{\mathrm{vir},4} = 0.2501^{+0.0018}_{-0.0016},$$
$$\log_{10} f_{\mathrm{X}} = 0.5007^{+0.0076}_{-0.0069},$$
$$\log_{10} \zeta_{\mathrm{ERB}} = -1.2666^{+0.0224}_{-0.0246}.$$

The best-fitting 21-cm signal corresponding to the parameters above, 90% confidence interval and its comparison with the EDGES signal are shown in figure 4 for PBHs of mass 10^{15} g. Using the definition of goodness-of-fit given in eq. (4.3) we get $\chi^2/\mathrm{dof} = 295.3/118$. The data thus prefer the model in which X-ray heating accompanies heating due to PBH evaporation; we discuss this point in the next section. The marginalised two-dimensional and one-dimensional posterior distributions for PBH mass of $M_{\mathrm{PBH}} = 10^{15}$ g is shown in figure 5. We see that in the presence of X-rays, only an upper bound is

Figure 4: Red curve shows the derived posterior median 21-cm signal in the presence of an X-ray background. The blue shaded region shows the 90% confidence intervals (CI). This is for PBH of mass 10^{15} g, and corresponds to $f_{\mathrm{PBH}} = 10^{-9.73}$ (95% level). The EDGES measurement is shown by the black dashed curve, with the grey shaded region around it showing the uncertainty. The goodness-of-fit is $\chi^2/\mathrm{dof} = 295.3/118$, which is much better compared to case I results.

obtained on $\log_{10} f_{\mathrm{PBH}}$. The model is consistent with the data in the absence of PBHs. We quantify our upper bounds by choosing 95% levels of the probability distribution of $\log_{10} f_{\mathrm{PBH}}$.

On comparing the best-fitting parameters for the two cases that are only related to setting the depth of the absorption, f_α and ζ_{ERB}, we find that in case I the values are higher. The Ly α background required in the absence of X-ray background is nearly 10 times higher in the presence of it. This is understandable because in case II X-ray takes care of the shape which then reduces the requirement of a stronger Ly α coupling or excess radio background. The minimum virial temperature is roughly the same in both cases because its job is mainly in setting the timing of the first drop in the signal.

Figure 6 shows our constraints on f_{PBH} as a function of PBH mass. For comparison we also show the results from previous literature [Clark et al. (2018), 84] (black dashed and dotted lines) which are somewhat weaker than ours, the reasons for which are discussed in the next section. We see that on log-log scale f_{PBH} vs M_{PBH} is approximately a straight line. In absence of X-ray heating we get

$$f_{\mathrm{PBH}} = 10^{-6.84} \left(\frac{M_{\mathrm{PBH}}}{10^{15}\,\mathrm{g}} \right)^{3.75} , \tag{5.1}$$
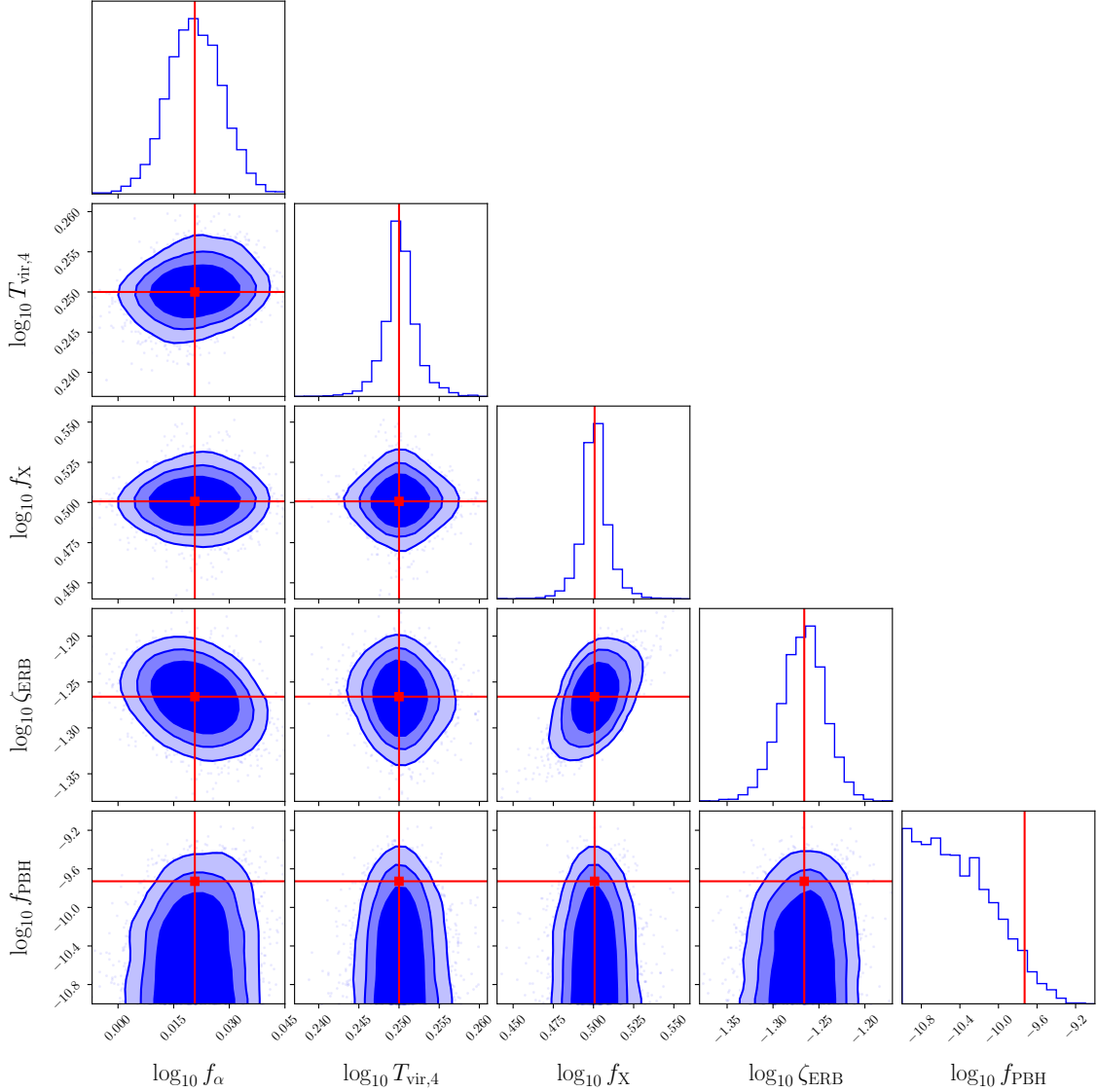
Figure 5: Marginalised posterior distributions of parameters for a PBH of mass $M_{\mathrm{PBH}} = 10^{15}\,\mathrm{g}$ in the presence of an X-ray background. The contour lines show the 68.3%, 86.6% and 95.5% levels corresponding to 1-sigma, 1.5-sigma and 2-sigma, respectively. The red lines show the median of the probability distribution except in case of $\log_{10} f_{\mathrm{PBH}}$, for which we show the 95% level.

with ~ 0.01 uncertainty (90%) on $\log_{10} f_{\mathrm{PBH}}$ (for all M_{PBH}) while in presence of X-ray heating

$$f_{\mathrm{PBH}} \leqslant 10^{-9.73} \left(\frac{M_{\mathrm{PBH}}}{10^{15}\,\mathrm{g}} \right)^{3.96}. \tag{5.2}$$

Figure 7 provides a consolidated view of the existing constraints on the fraction of DM composed of ultralight PBHs in the mass range of 10^{15}–$10^{17}\,\mathrm{g}$. This includes constraints obtained from the Planck measurement of CMB [69–73], electron/positron flux measurements by Voyager [65], measurement of the 511 keV line by SPI/INTEGRAL [58, 66, 67], measurement of the extra-galactic gamma-ray emission (EGB) by COMPTEL, SMM [59–61], Galactic Centre MeV gamma-ray measurements by INTEGRAL & COMPTEL [62, 63], diffuse supernovae neutrino background searches at the Super-
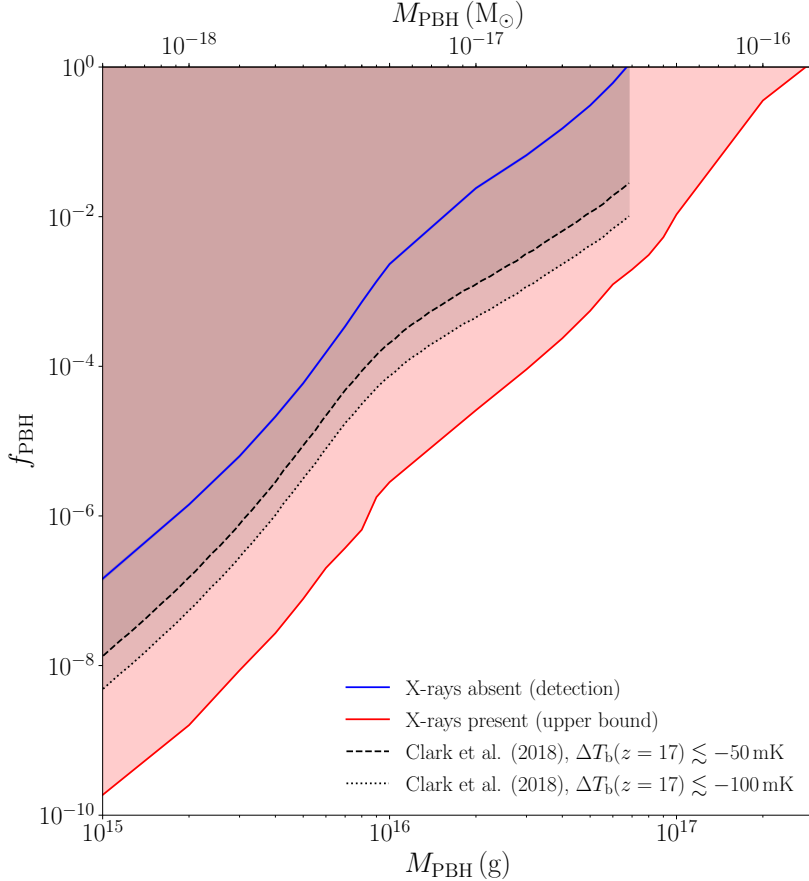
Figure 6: Our inferred constraints on the fraction of DM that is in the form of ultralight non-rotating PBHs. In the model with X-rays, the upper limit obtained from this analysis is shown by the red curve; the red shaded region is ruled out. In the model without X-rays, PBHs are the only heating mechanism, so the constraints formally represent a detection of PBHs. This is shown by the blue curve. (The associated uncertainty is too small to be visible on this plot.) For comparison, we also show the result from ref. [84] for $\Delta T_{\rm b}(z = 17) \lesssim -50\,{\rm mK}$ and $\Delta T_{\rm b}(z = 17) \lesssim -100\,{\rm mK}$ by black dashed and black dotted line, respectively.

Kamiokande neutrino observatory [58] and Leo T heating [74, 75]. (Appendix A lists the numerical values of our inferred constraints.)

5.3 Constraints on the primordial curvature power spectrum

If PBHs form due to the collapse of large density perturbations in the very early Universe, exclusion limits on the PBH abundance can be translated to the constraints on the primordial curvature power spectrum [164–167]. This leads to constraints on the primordial curvature power spectrum at small scales that are inaccessible to any other cosmological observable.

In gravitational collapse a certain fraction of the horizon mass collapses and forms PBHs. If all the PBHs formed at the same epoch, say in a radiation dominated era with a monochromatic mass distribution, we can relate their mass to the present day horizon mass, $M_0 = c^3/(2G_{\rm N}H_0)$,

$$M_{\rm PBH} = \gamma \sqrt{\Omega_{\rm r}}\, M_0 \left(\frac{g_0}{g_{\rm i}}\right)^{1/6} \left(\frac{H_0}{ck}\right)^2 , \qquad (5.3)$$
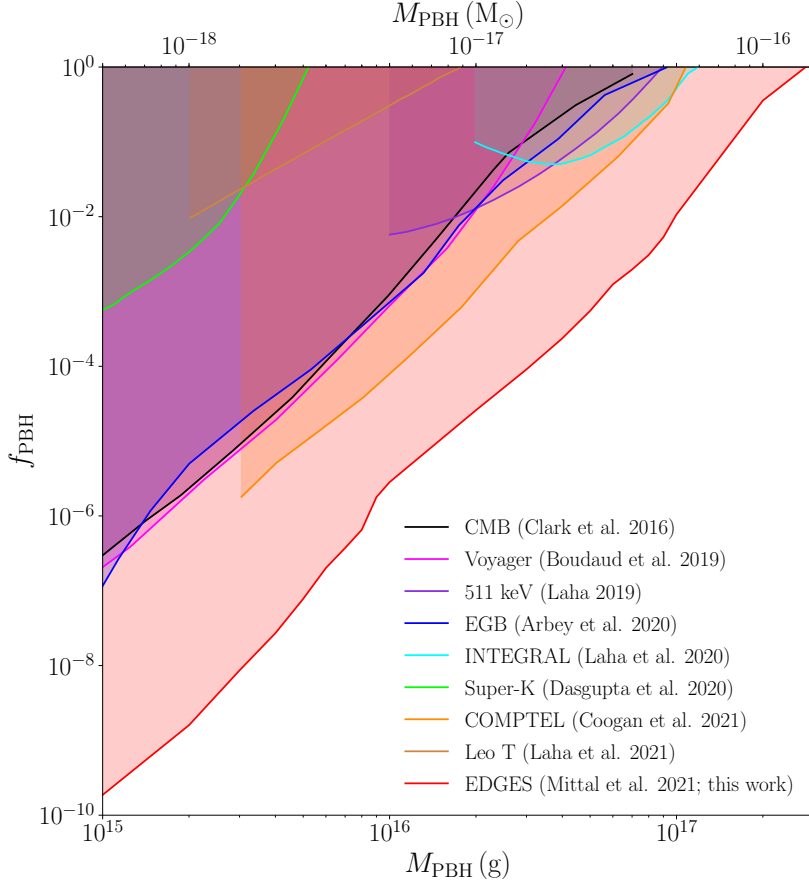
Figure 7: Constraints on the fraction of DM that is in the form of ultralight non-rotating PBHs. The exclusion limit obtained from this analysis is shown by the red line; the red shaded region is ruled out. Other exclusion limits, shown for comparison, are from the Planck measurement of CMB (black) [69], Voyager measurement of the positron flux (magenta) [65], SPI/INTEGRAL measurement of the 511 keV emission line (purple) [67], measurement of the EGB (blue) [60], INTEGRAL (cyan) & COMPTEL (orange) measurements of the Galactic-centre MeV gamma-ray flux [62, 63], diffuse supernovae neutrino background searches at Super-Kamiokande (green) [58] and Leo T heating (brown) [75].

where $\gamma \approx 0.2$ is the fraction of collapsed horizon mass [166, 168], $\Omega_{\rm r} \approx 9 \times 10^{-5}$ is the present day radiation density relative to critical density, k denotes scale of horizon re-entry and $g_0 = 3.38$ ($g_{\rm i} = 106.75$) denotes the total number relativistic degrees of freedom at present day (at the time of PBH formation) [169].

The initial mass fraction β of PBHs, is related to the present day PBH fraction of DM ($f_{\rm PBH}$) through [166]

$$\beta(M_{\rm PBH}) = f_{\rm PBH} \left(\frac{g_{\rm i}}{g_0} \right)^{1/4} \left(\frac{\Omega_{\rm DM}}{\Omega_{\rm r}^{3/4}} \right) \sqrt{\frac{M_{\rm PBH}}{\gamma M_0}} \, . \tag{5.4}$$

Note that, an assumption made in order to arrive at eqs. (5.3) and (5.4) is that the effective degrees of freedom for entropy are equal to that of energy (cf. ref. [167]).

In Press-Schechter theory [111], the initial mass fraction of PBHs is equivalent to the probability that the smoothed density field exceeds its threshold $\delta_{\rm c} \approx 0.42$ [170]. Therefore, β can also be written

as

$$\beta(M_{\rm PBH}) = 2 \int_{\delta_{\rm c}}^{1} \Pi(\delta) \, {\rm d}\delta \approx {\rm erfc}\left(\frac{\delta_{\rm c}}{\sqrt{2}\sigma}\right), \tag{5.5}$$

where $\Pi(\delta)$ denotes the probability density of the density contrast $\delta = \delta(R)$ for a comoving length scale R. The probability density is assumed to be a Gaussian of variance $\sigma^2 = \sigma^2(R)$ which can be written in terms of curvature power spectrum $\mathcal{P}_{\mathcal{R}}$ as [165]

$$\sigma^2 = \frac{16}{3} \int_0^\infty (kR)^2 j_1^2\left(\frac{kR}{\sqrt{3}}\right) {\rm e}^{-(kR)^2} \mathcal{P}_{\mathcal{R}}(k) \frac{{\rm d}k}{k}. \tag{5.6}$$

Assuming that the integral in the expression of mass variance σ is dominated at $kR \sim 1$ we can estimate the curvature power spectrum as

$$\mathcal{P}_{\mathcal{R}}(k) \approx \frac{3{\rm e}}{16} j_1^{-2}\left(\frac{1}{\sqrt{3}}\right) \sigma^2, \tag{5.7}$$

where

$$j_1(x) = \frac{\sin x - x\cos x}{x^2}, \tag{5.8}$$

is the spherical Bessel function.

For a PBH of mass $M_{\rm PBH}$ we know $f_{\rm PBH}$, then using eq. (5.4) we can calculate β. Using this β in eq. (5.5), we can find σ. Using the latter in eq. (5.7) gives us $\mathcal{P}_{\mathcal{R}}$. We now have $\mathcal{P}_{\mathcal{R}}$ as function of $M_{\rm PBH}$. To get $\mathcal{P}_{\mathcal{R}}$ as a function of k we finally use eq. (5.3). Our resulting constraints on the curvature power spectrum corresponding to case II (X-ray heating included) can be approximated as

$$\mathcal{P}_{\mathcal{R}}(k) \leqslant 2.46 \times 10^{-2} \left(\frac{k}{10^{15}\,{\rm Mpc}^{-1}}\right)^{n_{\mathcal{R}}-1}, \tag{5.9}$$

where $n_{\mathcal{R}} \approx 0.806$. Our result along with power spectrum constraints corresponding to other abundance constraints (shown in figure 7) are shown in figure 8.

6   Discussion

Models in which IGM heating is predominantly caused by PBHs predict a qualitatively different thermal history than those in which X-ray heating is dominant. Figure 9 shows the contribution to the IGM heating rate by different PBH masses and $f_{\rm PBH}$. This is shown in comparison with X-ray heating for $\log_{10} f_{\rm X} = 0.5$. X-ray production follows the build-up of dark matter haloes. Consequently, the X-ray heating rate builds up rather rapidly with time. In contrast, PBH heating rate is relatively constant with redshift. The 21-cm absorption signal measured by EDGES has a rapidly rising profile (it changes by $\sim 500\,{\rm mK}$ between $z = 17$ and 15). PBH-driven models are not capable of reproducing such steep absorption signals because increasing the PBH emissivity at lower redshift also increases it at higher redshifts, thereby weakening the signal itself. Models with X-rays are much better in explaining the steep rising edge of the observed absorption profile. This explains why the best-fitting model in figure 4 is a better fit to the data than the best-fitting model in figure 3.

This difference between the PBH-induced and X-ray-induced heating rates also helps understand why we only obtain an upper bound on the PBH fraction in the presence of X-rays. The model prefers to explain the rising edge of the absorption feature by means of X-ray emission because enhanced heating by PBHs worsens the signal as a whole due to excess heating at higher redshifts. Stated differently, in the presence of X-ray heating, HR heating does not offer any extra feature that can reduce the tension between the data and the model, which in turn means that all values of $f_{\rm PBH}$ below a certain maximum are allowed.

The contrast between our inferred constraints, as shown in figure 6, and constraints previously reported in the literature [84] illustrate the importance of using the full information content of the data. Constraints reported in ref. [84] were obtained by requiring that the value of the signal $\Delta T_{\rm b}$ remains
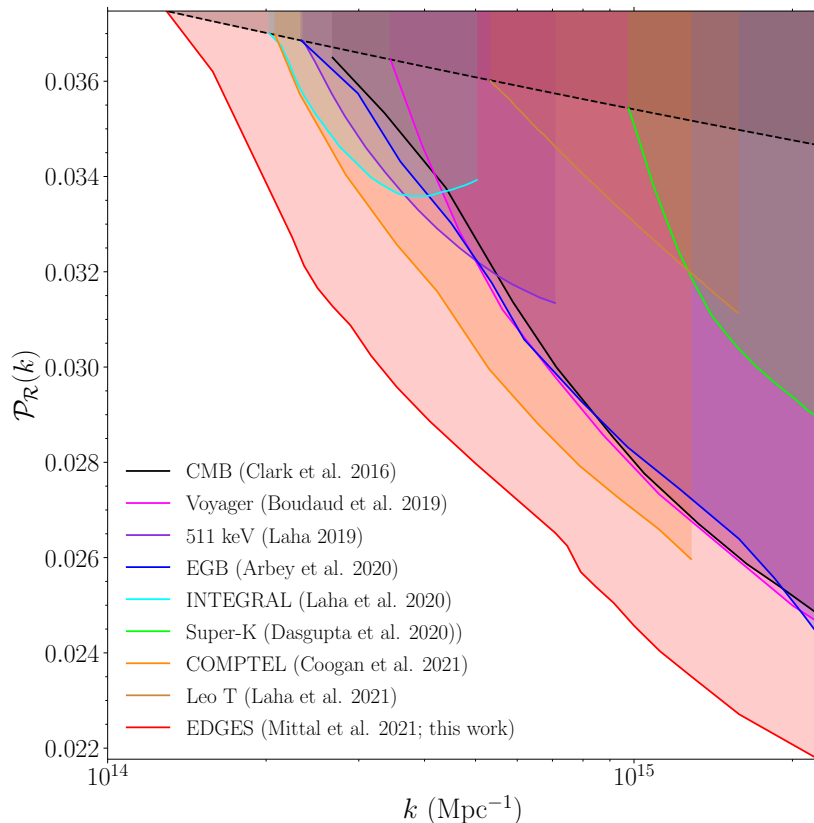
Figure 8: Upper limits (red curve) on the curvature power spectrum by translating our upper limits on f_{PBH} in the presence of X-ray heating. The red shaded region is ruled out. Constraints translated from the Planck measurement of CMB (black) [69], Voyager measurement of the positron flux (magenta) [65], SPI/INTEGRAL measurement of the 511 keV emission line (purple) [67], measurement of the EGB (blue) [60], INTEGRAL (cyan) & COMPTEL (orange) measurements of the Galactic-centre MeV gamma-ray flux [62, 63], diffuse supernovae neutrino background searches at Super-Kamiokande (green) [58] and Leo T heating (brown) [75] are also shown for comparison. The region above the black dashed line is ruled out because in that region the density of PBHs exceeds that of DM i.e. $f_{\text{PBH}} > 1$.

below a somewhat arbitrarily chosen threshold of -50 or $-100\,\text{mK}$ at $z = 17$, which was taken to be the approximate mid-point of the absorption profile detected by EDGES. In their 'standard model', which had no PBH heating, $\Delta T_{\text{b}}(z = 17) = -200\,\text{mK}$. A PBH scenario that led to heating rates that raise ΔT_{b} to values greater than -50 or $-100\,\text{mK}$ was deemed to be ruled out by the EDGES data. But the data are richer than this. In general, the three main features in the observed profile are its location, depth and width. If we use all available redshift points from the data, as we do in this work, there are more features to exploit, e.g., the steepness of the rise and fall of the absorption feature. Utilising all of this information is particularly advantageous for heating mechanisms that evolve slowly, such as PBHs. This explains why the constraints from our analysis, shown in figure 6, are tighter than those previously reported in the literature.

Other papers that have done a parameter study include references such as [27, 130, 131, 136, 161]. Our choice of parameters is more or less similar to those considered in refs. [27, 130, 131]. These
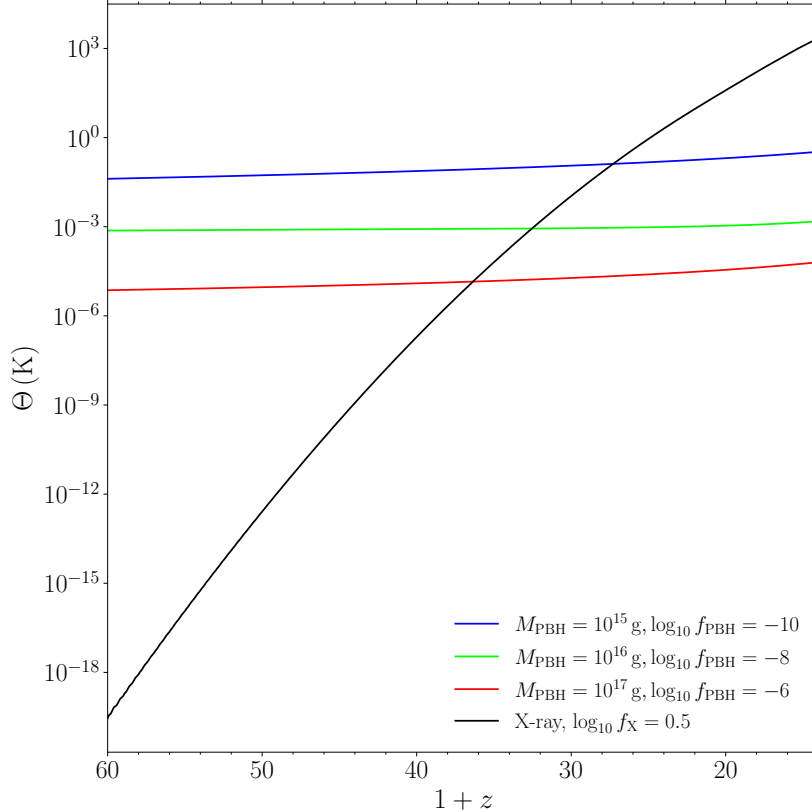
Figure 9: A comparison of the heating rate due to PBH with that due to X-rays in our model. The heating rate is expressed here in units of temperature as $\Theta = 2q \cdot [3n_b k_B H(z)]^{-1}$. The blue, green and red solid lines shows HR heating for different combinations of M_{PBH} and f_{PBH}. The slow rise seen in Θ_{HR} is dominantly because of $H(z)$ as $q_{HR,heat}$ remains constant (since $f_c(E_K, z)$ has a weak dependence on z). The black solid line shows X-ray heating for $\log_{10} f_X = 0.5$. Because X-ray emission traces halo formation, X-ray heating rises more sharply than PBH-induced heating.

authors study seven-parameter models with parameters $f_\star, V_c, f_X, \nu_{min}, \alpha, \tau_e$ and R_{mfp} that represent the star formation efficiency, minimum virial circular velocity of star-forming haloes, X-ray heating efficiency, low frequency cut-off of the X-ray SED, slope of X-ray SED, electron scattering optical depth and mean-free path of ionizing photons, respectively. In this work, we did not treat $f_\star$ as a free parameter due to its degeneracy with f_α and f_X. The parameter V_c is present in our analysis as T_{vir} for setting the minimum halo mass for star formation [112, 113]. The parameter f_X is present in our analysis as well. The other two parameters related to X-ray SED, ν_{min}, (quantified by energy, E_0, instead of frequency) and α (denoted by w in this work) are kept fixed here due to degeneracy with f_X in the case of ν_{min} and weak dependence in the case of α, as discussed in section 2.2.3. The other two parameters used in the literature, τ_e and R_{mfp}, are not present in our analysis as we exclusively study the 21-cm signal at Cosmic Dawn, when the effects of reionization are absent. The parameter f_α was not present in previous papers. The advantage of f_α is to scale up Ly α background without affecting other physics. The minimum T_{vir} also changes Ly α background but then it simultaneously affects X-ray background also. The other extra parameter ζ_{ERB} is specific to the work that have considered an excess radio (denoted by ξ and A_r in ref. [26] and [27], respectively).

While this choice of parameters may be conservative, it is justified to ask if other parametrizations are possible. Because little is known about the astrophysics at these redshifts, particularly in the presence of exotic processes such as PBH physics, a wide range of alternative parametrizations can be potentially considered. This 'model selection' question is unfortunately out of the scope of this paper due to the possible diversity of models. We leave its study for future work.

7 Conclusions

We inferred constraints on the abundance of uncharged non-rotating primordial black holes (PBHs), assuming a monochromatic distribution in PBH masses, in the mass range $\sim 10^{15}$–10^{17} g using the global 21-cm signal measured by EDGES. Our main conclusions are:

1. In the absence of X-ray heating, PBH evaporation is the only major heating mechanism in our model. In this scenario, the EDGES measurement formally represents a detection of PBHs. For a 10^{15} g PBH we infer a best-fitting value of the fraction of dark matter that is in the form of PBHs as $\log_{10} f_{\rm PBH} = -6.84 \pm 0.02$. The fraction $f_{\rm PBH}$ changes as $\sim M_{\rm PBH}^{3.75}$ at higher PBH masses (eq. 5.1 and figure 6). However, note that the best-fitting values in this scenario are ruled out by Voyager, EGB and CMB measurements, thus favouring our model with X-ray heating.

2. When X-ray heating is present, we get only an upper bound on the fraction of DM in the form of PBHs. But we find that the data favour this scenario because the X-ray heating rate evolves much more rapidly than the heating rate induced by PBH evaporation. For a 10^{15} g PBH we infer $\log_{10} f_{\rm PBH} \leqslant -9.73$ ($95^{\rm th}$ percentile). The fraction $f_{\rm PBH}$ changes as $\sim M_{\rm PBH}^{3.96}$ towards higher PBH masses (eq. 5.2 and figure 6).

3. Our constraints on $f_{\rm PBH}$ are the strongest yet for the PBH mass range of $\sim 10^{15}$–10^{17} g. An important reason behind this is that we use the measured 21-cm signal values across the EDGES band. This tightens the limits on PBH evaporation because PBH-induced heating rate evolves very little across the redshift range covered by EDGES.

4. Our inferred values for the non-PBH astrophysical parameters are consistent with observations as well as other analyses. The best-fitting normalisation of Lyman-α emissivity is 1, i.e. $f_\alpha \approx 1$ which also corresponds to our base model of Population II type stars. Similarly, we have $f_{\rm X} \approx 3$ in which our base model normalisation corresponds to $L_{\rm X}$-SFR relation observed for high mass X-ray binaries. The minimum virial temperature required for estimating star formation rate density in Press-Schechter formalism is $T_{\rm vir} \approx 1.8 \times 10^4$ K, which is close to the atomic cooling limit. Finally, we require an excess radio background quantified by $\zeta_{\rm ERB} \approx 0.05$, where $\zeta_{\rm ERB} = 1$ corresponds to the maximum observed by ARCADE 2/LWA1.

5. We also derived bounds on the curvature power spectrum at extremely small scales under the assumption of a spherical gravitational collapse based on the Press-Schechter formalism. We get an upper limit of $\mathcal{P}_{\mathcal{R}} = 2.46 \times 10^{-2}$ at $k = 10^{15}$ Mpc^{-1}, with a $\sim k^{-0.2}$ scaling at other values of k (eq. 5.9 and figure 8).

This work highlights the usefulness of the global 21-cm signal for probing exotic physical processes. It also shows that global 21-cm measurements contain much more crucially useful information than just the redshift of absorption. The large number of experiments currently underway to probe the 21-cm signal add to the promise of this type of study in future.

Acknowledgments

References

[1] P. Madau, A. Meiksin and M.J. Rees, *21 centimeter tomography of the intergalactic medium at high redshift*, *Astrophys. J.* **475** (1997) 429.

[2] S.P. Oh and K.J. Mack, *Foregrounds for 21-cm observations of neutral gas at high redshift*, *Mon. Not. R. Astron. Soc.* **346** (2003) 871.

[3] A. De Oliveira-Costa, M. Tegmark, B.M. Gaensler, J. Jonas, T.L. Landecker and P. Reich, *A model of diffuse Galactic radio emission from 10 MHz to 100 GHz*, *Mon. Not. R. Astron. Soc.* **388** (2008) 247.

[4] G. Bernardi, A.G. de Bruyn, M.A. Brentjens, B. Ciardi, G. Harker, V. Jelić et al., *Foregrounds for observations of the cosmological 21 cm line - I. First Westerbork measurements of Galactic emission at 150 MHz in a low latitude field*, *Astron. Astrophys.* **500** (2009) 965.

[5] H. Zheng, M. Tegmark, J.S. Dillon, D.A. Kim, A. Liu, A.R. Neben et al., *An improved model of diffuse galactic radio emission from 10 MHz to 5 THz*, *Mon. Not. R. Astron. Soc.* **464** (2016) 3486.

[6] J.D. Bowman and A.E.E. Rogers, *A lower limit of $\Delta z > 0.06$ for the duration of the reionization epoch*, *Nature* **468** (2010) 796.

[7] J.D. Bowman, A.E.E. Rogers, R.A. Monsalve, T.J. Mozdzen and N. Mahesh, *An absorption profile centred at 78 megahertz in the sky-averaged spectrum*, *Nature* **555** (2018) 67.

[8] S.A. Wouthuysen, *On the excitation mechanism of the 21-cm (radio-frequency) interstellar hydrogen emission line.*, *Astron. J.* **57** (1952) 31.

[9] G.B. Field, *Excitation of the Hydrogen 21-CM Line*, *Proc. IRE* **46** (1958) 240.

[10] X. Chen and J. Miralda-Escudé, *The Spin–Kinetic Temperature Coupling and the Heating Rate due to Lyα Scattering before Reionization: Predictions for 21 Centimeter Emission and Absorption*, *Astrophys. J.* **602** (2004) 1.

[11] A. Meiksin, *Energy transfer by the scattering of resonant photons*, *Mon. Not. R. Astron. Soc.* **370** (2006) 2025.

[12] S.R. Furlanetto and J.R. Pritchard, *The scattering of Lyman-series photons in the intergalactic medium*, *Mon. Not. R. Astron. Soc.* **372** (2006) 1093.

[13] S. Mittal and G. Kulkarni, *Ly α coupling and heating at cosmic dawn*, *Mon. Not. R. Astron. Soc.* **503** (2020) 4264.

[14] T. Venumadhav, L. Dai, A. Kaurov and M. Zaldarriaga, *Heating of the intergalactic medium by the cosmic microwave background during cosmic dawn*, *Phys. Rev. D* **98** (2018) 103513.

[15] R. Weymann, *Diffusion Approximation for a Photon Gas Interacting with a Plasma via the Compton Effect*, *Phys. Fluids* **8** (1965) 2112.

[16] S.R. Furlanetto, *The global 21-centimeter background from high redshifts*, *Mon. Not. R. Astron. Soc.* **371** (2006) 867.

[17] A. Mesinger, A. Ferrara and D.S. Spiegel, *Signatures of X-rays in the early Universe*, *Mon. Not. R. Astron. Soc.* **431** (2013) 621.

[18] P. Christian and A. Loeb, *Measuring the X-ray background in the reionization era with first generation 21 cm experiments*, *JCAP* **2013** (2013) 14.

[19] A. Fialkov, A. Cohen, R. Barkana and J. Silk, *Constraining the redshifted 21-cm signal with the unresolved soft X-ray background*, *Mon. Not. R. Astron. Soc.* **464** (2016) 3498.

[20] F. Haardt and P. Madau, *Radiative Transfer in a Clumpy Universe. IV. New Synthesis Models of the Cosmic UV/X-Ray Background*, *Astrophys. J.* **746** (2012) 125.

[21] P. Madau and T. Fragos, *Radiation backgrounds at cosmic dawn: X-rays from compact binaries*, *Astrophys. J.* **840** (2017) 39.

[22] R. Barkana, *Possible interaction between baryons and dark-matter particles revealed by the first stars*, *Nature* **555** (2018) 71.

[23] J.B. Muñoz and A. Loeb, *A small amount of mini-charged dark matter could cool the baryons in the early universe*, *Nature* **557** (2018) 684.

[24] A. Berlin, D. Hooper, G. Krnjaic and S.D. McDermott, *Severely Constraining Dark-Matter Interpretations of the 21-cm Anomaly*, *Phys. Rev. Lett.* **121** (2018) 011102.

[25] H. Liu, N.J. Outmezguine, D. Redigolo and T. Volansky, *Reviving millicharged dark matter for 21-cm cosmology*, *Phys. Rev. D* **100** (2019) 123011.

[26] C. Feng and G. Holder, *Enhanced global signal of neutral hydrogen due to excess radiation at cosmic dawn*, *Astrophys. J.* **858** (2018) L17.

[27] A. Fialkov and R. Barkana, *Signature of excess radio background in the 21-cm global signal and power spectrum*, *Mon. Not. R. Astron. Soc.* **486** (2019) 1763.

[28] J. Dowell and G.B. Taylor, *The Radio Background below 100 MHz*, *Astrophys. J.* **858** (2018) L9.

[29] D.J. Fixsen, A. Kogut, S. Levin, M. Limon, P. Lubin, P. Mirel et al., *ARCADE 2 Measurement of the Absolute Sky Brightness at 3-90 GHz*, *Astrophys. J.* **734** (2011) 5.

[30] J. Singal, J. Haider, M. Ajello, D.R. Ballantyne, E. Bunn, J. Condon et al., *The radio synchrotron background: Conference summary and report*, *Publ. Astron. Soc. Pac.* **130** (2018) 036001.

[31] H. Tashiro and N. Sugiyama, *Probing primordial magnetic fields with the 21-cm fluctuations*, *Mon. Not. R. Astron. Soc.* **372** (2006) 1060.

[32] D.R.G. Schleicher, R. Banerjee and R.S. Klessen, *Influence of primordial magnetic fields on 21 cm emission*, *Astrophys. J.* **692** (2009) 236.

[33] K.E. Kunze, *21 cm line signal from magnetic modes*, *JCAP* **2019** (2019) 033.

[34] K.E. Kunze, *Tracing Primordial Magnetic Fields with 21 cm Line Observations*, *Galaxies* **7** (2019) 37.

[35] A. Bera, K.K. Datta and S. Samui, *Primordial magnetic fields during the cosmic dawn in light of EDGES 21-cm signal*, *Mon. Not. R. Astron. Soc.* **498** (2020) 918.

[36] P.K. Natwariya, *Constraint on primordial magnetic fields in the light of ARCADE 2 and EDGES observations*, *Eur. Phys. J. C* **81** (2021) 394.

[37] S. Bharadwaj and T.G. Sarkar, *Gravitational-wave detection using redshifted 21-cm observations*, *Phys. Rev. D* **79** (2009) 124003.

[38] C.M. Hirata, A. Mishra and T. Venumadhav, *Detecting primordial gravitational waves with circular polarization of the redshifted 21 cm line. I. Formalism*, *Phys. Rev. D* **97** (2018) 103521.

[39] A. Mishra and C.M. Hirata, *Detecting primordial gravitational waves with circular polarization of the redshifted 21 cm line. II. Forecasts*, *Phys. Rev. D* **97** (2018) 103522.

[40] M. Safarzadeh, E. Scannapieco and A. Babul, *A Limit on the Warm Dark Matter Particle Mass from the Redshifted 21 cm Absorption Line*, *Astrophys. J.* **859** (2018) L18.

[41] M. Sitwell, A. Mesinger, Y.-Z. Ma and K. Sigurdson, *The imprint of warm dark matter on the cosmological 21-cm signal*, *Mon. Not. R. Astron. Soc.* **438** (2014) 2664.

[42] A. Chatterjee, P. Dayal, T.R. Choudhury and A. Hutter, *Ruling out 3 keV warm dark matter using 21 cm EDGES data*, *Mon. Not. R. Astron. Soc.* **487** (2019) 3560.

[43] A. Boyarsky, D. Iakubovskyi, O. Ruchayskiy, A. Rudakovskyi and W. Valkenburg, *21-cm observations and warm dark matter models*, *Phys. Rev. D* **100** (2019) 123005.

[44] V. Vipp, A. Hektor and G. Hütsi, *Rapid onset of the 21-cm signal suggests a preferred mass range for dark matter particle*, *Phys. Rev. D* **103** (2021) 123002.

[45] S.R. Furlanetto, S.P. Oh and E. Pierpaoli, *Effects of dark matter decay and annihilation on the high-redshift 21 cm background*, *Phys. Rev. D* **74** (2006) 103502.

[46] M. Valdés, A. Ferrara, M. Mapelli and E. Ripamonti, *Constraining dark matter through 21-cm observations*, *Mon. Not. R. Astron. Soc.* **377** (2007) 245.

[47] G. D'Amico, P. Panci and A. Strumia, *Bounds on Dark-Matter Annihilations from 21-cm Data*, *Phys. Rev. Lett.* **121** (2018) 011103.

[48] H. Liu and T.R. Slatyer, *Implications of a 21-cm signal for dark matter annihilation and decay*, *Phys. Rev. D* **98** (2018) 023501.

[49] J.R. Bhatt, A.K. Mishra and A.C. Nayak, *Viscous dark matter and 21 cm cosmology*, *Phys. Rev. D* **100** (2019) 063539.

[50] Y.B. Zeldovich and I.D. Novikov, *The Hypothesis of Cores Retarded during Expansion and the Hot Cosmological Model*, *Astronomicheskii Zhurnal* **43** (1966) 758.

[51] S. Hawking, *Gravitationally collapsed objects of very low mass*, *Mon. Not. R. Astron. Soc.* **152** (1971) 75.

[52] G.F. Chapline, *Cosmological effects of primordial black holes*, *Nature* **253** (1975) 251.

[53] M.Y. Khlopov, *Primordial black holes*, *Res. Astron. Astrophys.* **10** (2010) 495.

[54] B. Carr and F. Kühnel, *Primordial Black Holes as Dark Matter: Recent Developments*, *Annu. Rev. Nucl. Part. Sci.* **70** (2020) 355.

[55] A.M. Green and B.J. Kavanagh, *Primordial black holes as a dark matter candidate*, *J. Phys. G* **48** (2021) 043001.

[56] B. Carr, K. Kohri, Y. Sendouda and J. Yokoyama, *Constraints on primordial black holes*, *Rep. Prog. Phys.* **84** (2021) 116902.

[57] P. Villanueva-Domingo, O. Mena and S. Palomares-Ruiz, *A Brief Review on Primordial Black Holes as Dark Matter*, *Front. Astron. Space Sci.* **8** (2021) 87.

[58] B. Dasgupta, R. Laha and A. Ray, *Neutrino and positron constraints on spinning primordial black hole dark matter*, *Phys. Rev. Lett.* **125** (2020) 101101.

[59] B.J. Carr, K. Kohri, Y. Sendouda and J. Yokoyama, *New cosmological constraints on primordial black holes*, *Phys. Rev. D* **81** (2010) 104019.

[60] A. Arbey, J. Auffinger and J. Silk, *Constraining primordial black hole masses with the isotropic gamma ray background*, *Phys. Rev. D* **101** (2020) 023010.

[61] G. Ballesteros, J. Coronado-Blázquez and D. Gaggero, *X-ray and gamma-ray limits on the primordial black hole abundance from Hawking radiation*, *Phys. Lett. B* **808** (2020) 135624.

[62] R. Laha, J.B. Muñoz and T.R. Slatyer, *INTEGRAL constraints on primordial black holes and particle dark matter*, *Phys. Rev. D* **101** (2020) 123514.

[63] A. Coogan, L. Morrison and S. Profumo, *Direct Detection of Hawking Radiation from Asteroid-Mass Primordial Black Holes*, *Phys. Rev. Lett.* **126** (2021) 171101.

[64] J. Iguaz, P.D. Serpico and T. Siegert, *Isotropic x-ray bound on primordial black hole dark matter*, *Phys. Rev. D* **103** (2021) 103025.

[65] M. Boudaud and M. Cirelli, *Voyager 1 $e^{\pm}$ Further Constrain Primordial Black Holes as Dark Matter*, *Phys. Rev. Lett.* **122** (2019) 041104.

[66] W. DeRocco and P.W. Graham, *Constraining Primordial Black Hole Abundance with the Galactic 511 keV Line*, *Phys. Rev. Lett.* **123** (2019) 251102.

[67] R. Laha, *Primordial Black Holes as a Dark Matter Candidate Are Severely Constrained by the Galactic Center 511 keV γ-Ray Line*, *Phys. Rev. Lett.* **123** (2019) 251101.

[68] R.-G. Cai, Y.-C. Ding, X.-Y. Yang and Y.-F. Zhou, *Constraints on a mixed model of dark matter particles and primordial black holes from the galactic 511 keV line*, *JCAP* **2021** (2021) 057.

[69] S.J. Clark, B. Dutta, Y. Gao, L.E. Strigari and S. Watson, *Planck constraint on relic primordial black holes*, *Phys. Rev. D* **95** (2017) 083006.

[70] P. Stöcker, M. Krämer, J. Lesgourgues and V. Poulin, *Exotic energy injection with ExoCLASS: application to the Higgs portal model and evaporating black holes*, *JCAP* **03** (2018) 018.

[71] H. Poulter, Y. Ali-Haïmoud, J. Hamann, M. White and A.G. Williams, *CMB constraints on ultra-light primordial black holes with extended mass distributions*, `1907.06485`.

[72] S.K. Acharya and R. Khatri, *CMB and BBN constraints on evaporating primordial black holes revisited*, *JCAP* **06** (2020) 018.

[73] J. Cang, Y. Gao and Y.-Z. Ma, *Prospects of future CMB anisotropy probes for primordial black holes*, *JCAP* **2021** (2021) 051.

[74] H. Kim, *A constraint on light primordial black holes from the interstellar medium temperature*, *Mon. Not. R. Astron. Soc.* **504** (2021) 5475.

[75] R. Laha, P. Lu and V. Takhistov, *Gas heating from spinning and non-spinning evaporating primordial black holes*, *Phys. Lett. B* **820** (2021) 136459.

[76] M.H. Chan and C.M. Lee, *Constraining Primordial Black Hole Fraction at the Galactic Centre using radio observational data*, *Mon. Not. R. Astron. Soc.* **497** (2020) 1212.

[77] B. Dutta, A. Kar and L.E. Strigari, *Constraints on MeV dark matter and primordial black holes: Inverse Compton signals at the SKA*, *JCAP* **03** (2021) 011.

[78] A. Ray, R. Laha, J.B. Muñoz and R. Caputo, *Near future MeV telescopes can discover asteroid-mass primordial black hole dark matter*, *Phys. Rev. D* **104** (2021) 023516.

[79] S. Wang, D.-M. Xia, X. Zhang, S. Zhou and Z. Chang, *Constraining primordial black holes as dark matter at JUNO*, *Phys. Rev. D* **103** (2021) 043010.

[80] R. Calabrese, D.F.G. Fiorillo, G. Miele, S. Morisi and A. Palazzo, *Primordial Black Hole Dark Matter evaporating on the Neutrino Floor*, `2106.02492`.

[81] V.D. Romeri, P. Martínez-Miravé and M. Tórtola, *Signatures of primordial black hole dark matter at DUNE and THEIA*, *JCAP* **2021** (2021) 051.

[82] K.J. Mack and D.H. Wesley, *Primordial black holes in the Dark Ages: Observational prospects for future 21cm surveys*, `0805.1531`.

[83] A. Hektor, G. Hütsi, L. Marzola, M. Raidal, V. Vaskonen and H. Veermäe, *Constraining primordial black holes with the EDGES 21-cm absorption signal*, *Phys. Rev. D* **98** (2018) 023503.

[84] S.J. Clark, B. Dutta, Y. Gao, Y.-Z. Ma and L.E. Strigari, *21 cm limits on decaying dark matter and primordial black holes*, *Phys. Rev. D* **98** (2018) 043006.

[85] O. Mena, S. Palomares-Ruiz, P. Villanueva-Domingo and S.J. Witte, *Constraining the primordial black hole abundance with 21-cm cosmology*, *Phys. Rev. D* **100** (2019) 043540.

[86] Y. Yang, *The abundance of primordial black holes from the global 21cm signal and extragalactic gamma-ray background*, *Eur. Phys. J. Plus* **135** (2020) 690.

[87] A. Halder and S. Banerjee, *Bounds on abundance of primordial black hole and dark matter from EDGES 21-cm signal*, *Phys. Rev. D* **103** (2021) 063044.

[88] H. Tashiro and K. Kadota, *Constraining mixed dark-matter scenarios of WIMPs and primordial black holes from CMB and 21-cm observations*, *Phys. Rev. D* **103** (2021) 123532.

[89] H. Tashiro and K. Kadota, *CMB and 21-cm bounds on early structure formation boosted by primordial black hole entropy fluctuations*, *Phys. Rev. D* **104** (2021) 063522.

[90] D.J. Fixsen, *The Temperature of the Cosmic Microwave Background*, *Astrophys. J.* **707** (2009) 916.

[91] Planck Collaboration, N. Aghanim, Y. Akrami, M. Ashdown, J. Aumont, C. Baccigalupi et al., *Planck 2018 results - VI. Cosmological parameters*, *Astron. Astrophys.* **641** (2020) A6.

[92] S.R. Furlanetto, S. Peng Oh and F.H. Briggs, *Cosmology at low frequencies: The 21 cm transition and the high-redshift universe*, *Phys. Rep.* **433** (2006) 181.

[93] J.R. Pritchard and A. Loeb, *21 cm cosmology in the 21st century*, *Rep. Prog. Phys.* **75** (2012) 086901.

[94] R. Barkana, *The rise of the first stars: Supersonic streaming, radiative feedback, and 21-cm cosmology*, *Phys. Rep.* **645** (2016) 1.

[95] A. Mesinger, ed., *The Cosmic 21-cm Revolution*, 2514-3433, IOP Publishing (2019), 10.1088/2514-3433/ab4a73.

[96] A. Liu and J.R. Shaw, *Data Analysis for Precision 21 cm Cosmology*, *Publ. Astron. Soc. Pac.* **132** (2020) 062001.

[97] H.I. Ewen and E.M. Purcell, *Observation of a Line in the Galactic Radio Spectrum: Radiation from Galactic Hydrogen at 1,420 Mc./sec.*, *Nature* **168** (1951) 356.

[98] A. Mesinger, S. Furlanetto and R. Cen, *21CMFAST: a fast, seminumerical simulation of the high-redshift 21-cm signal*, *Mon. Not. R. Astron. Soc.* **411** (2011) 955.

[99] R. Barkana and A. Loeb, *Detecting the earliest galaxies through two new sources of 21 centimeter fluctuations*, *Astrophys. J.* **626** (2005) 1.

[100] J.P. Wild, *The Radio-Frequency Line Spectrum of Atomic Hydrogen and its Applications in Astronomy*, *Astrophys. J.* **115** (1952) 206.

[101] A.C. Allison and A. Dalgarno, *Spin Change in Collisions of Hydrogen Atoms*, *Astrophys. J.* **158** (1969) 423.

[102] B. Zygelman, *Hyperfine Level–changing Collisions of Hydrogen Atoms and Tomography of the Dark Age Universe*, *Astrophys. J.* **622** (2005) 1356.

[103] S.R. Furlanetto and M.R. Furlanetto, *Spin-exchange rates in electron–hydrogen collisions*, *Mon. Not. R. Astron. Soc.* **374** (2006) 547.

[104] H. Liszt, *The spin temperature of warm interstellar H I*, *Astron. Astrophys.* **371** (2001) 698.

[105] M. Kuhlen, P. Madau and R. Montgomery, *The spin temperature and 21 cm brightness of the intergalactic medium in the pre-reionization era*, *Astrophys. J.* **637** (2006) L1.

[106] S.R. Furlanetto and M.R. Furlanetto, *Spin exchange rates in proton–hydrogen collisions*, *Mon. Not. R. Astron. Soc.* **379** (2007) 130.

[107] G.B. Arfken, H.J. Weber and F.E. Harris, *Mathematical Methods for Physicists*, Academic Press, 7 ed. (2013), 10.1016/C2009-0-30629-7.

[108] G.B. Rybicki and I.P. dell'Antonio, *The Time Development of a Resonance Line in the Expanding Universe*, *Astrophys. J.* **427** (1994) 603.

[109] J.E. Gunn and B.A. Peterson, *On the Density of Neutral Hydrogen in Intergalactic Space.*, *Astrophys. J.* **142** (1965) 1633.

[110] Y. Ali-Haïmoud, P.D. Meerburg and S. Yuan, *New light on 21 cm intensity fluctuations from the dark ages*, *Phys. Rev. D* **89** (2014) 083506.

[111] W.H. Press and P. Schechter, *Formation of Galaxies and Clusters of Galaxies by Self-Similar Gravitational Condensation*, *Astrophys. J.* **187** (1974) 425.

[112] R. Barkana and A. Loeb, *In the beginning: the first sources of light and the reionization of the universe*, *Phys. Rep.* **349** (2001) 125.

[113] P. Dayal and A. Ferrara, *Early galaxy formation and its large-scale effects*, *Phys. Rep.* **780-782** (2018) 1.

[114] B. Diemer, *COLOSSUS: A python toolkit for cosmology, large-scale structure, and dark matter halos*, *Astrophys. J. Suppl. Ser.* **239** (2018) 35.

[115] C.M. Hirata, *Wouthuysen-Field coupling strength and application to high-redshift 21-cm radiation*, *Mon. Not. R. Astron. Soc.* **367** (2006) 259.

[116] J.R. Pritchard and S.R. Furlanetto, *Descending from on high: Lyman-series cascades and spin-kinetic temperature coupling in the 21-cm line*, *Mon. Not. R. Astron. Soc.* **367** (2006) 1057.

[117] S. Seager, D.D. Sasselov and D. Scott, *A New Calculation of the Recombination Epoch*, *Astrophys. J.* **523** (1999) L1.

[118] S. Seager, D.D. Sasselov and D. Scott, *How exactly did the universe become neutral?*, *Astrophys. J. Suppl. Ser.* **128** (2000) 407.

[119] J.S.B. Wyithe and A. Loeb, *Reionization of Hydrogen and Helium by Early Stars and Quasars*, *Astrophys. J.* **586** (2003) 693.

[120] R. Barkana and A. Loeb, *Unusually Large Fluctuations in the Statistics of Galaxy Formation at High Redshift*, *Astrophys. J.* **609** (2004) 474.

[121] I.F. Mirabel, M. Dijkstra, P. Laurent, A. Loeb and J.R. Pritchard, *Stellar black holes at the dawn of the universe*, *Astron. Astrophys.* **528** (2011) A149.

[122] C. Power, G. James, C. Combet and G. Wynn, *Feedback from High-mass X-Ray Binaries on the High-redshift Intergalactic Medium: Model Spectra*, *Astrophys. J.* **764** (2013) 76.

[123] T. Fragos, B.D. Lehmer, S. Naoz, A. Zezas and A. Basu-Zych, *Energy Feedback from X-Ray Binaries in the Early Universe*, *Astrophys. J.* **776** (2013) L31.

[124] S.P. Oh, *Reionization by hard photons. I. X-rays from the first star clusters*, *Astrophys. J.* **553** (2001) 499.

[125] P. Madau, M.J. Rees, M. Volonteri, F. Haardt and S.P. Oh, *Early reionization by miniquasars*, *Astrophys. J.* **604** (2004) 484.

[126] T.M. Tauris and E.P.J. van den Heuvel, *Formation and evolution of compact stellar X-ray sources*, in *Compact Stellar X-ray Sources*, W. Lewin and M. van der Klis, eds., Cambridge Astrophysics, p. 623–666, Cambridge University Press (2006), DOI.

[127] G. Fabbiano, *Populations of X-ray sources in galaxies*, *Annu. Rev. Astron. Astr.* **44** (2006) 323.

[128] M. Brorby, P. Kaaret, A. Prestwich and I.F. Mirabel, *Enhanced X-ray emission from Lyman break analogues and a possible L_X–SFR–metallicity plane*, *Mon. Not. R. Astron. Soc.* **457** (2016) 4081.

[129] B.D. Lehmer, A.R. Basu-Zych, S. Mineo, W.N. Brandt, R.T. Eufrasio, T. Fragos et al., *The Evolution of Normal Galaxy X-Ray Emission through Cosmic History: Constraints from the 6 MS Chandra Deep Field-South*, *Astrophys. J.* **825** (2016) 7.

[130] A. Cohen, A. Fialkov, R. Barkana and M. Lotem, *Charting the parameter space of the global 21-cm signal*, *Mon. Not. R. Astron. Soc.* **472** (2017) 1915.

[131] R.A. Monsalve, A. Fialkov, J.D. Bowman, A.E.E. Rogers, T.J. Mozdzen, A. Cohen et al., *Results from EDGES high-band. III. new constraints on parameters of the early universe*, *Astrophys. J.* **875** (2019) 67.

[132] H.-J. Grimm, M. Gilfanov and R. Sunyaev, *High-mass X-ray binaries as a star formation rate indicator in distant galaxies*, *Mon. Not. R. Astron. Soc.* **339** (2003) 793.

[133] M. Gilfanov, H.-J. Grimm and R. Sunyaev, *L_X-SFR relation in star-forming galaxies*, *Mon. Not. R. Astron. Soc.* **347** (2004) L57.

[134] S. Mineo, M. Gilfanov and R. Sunyaev, *X-ray emission from star-forming galaxies – I. High-mass X-ray binaries*, *Mon. Not. R. Astron. Soc.* **419** (2012) 2095.

[135] J. Mirocha, *Decoding the X-ray properties of pre-reionization era sources*, *Mon. Not. R. Astron. Soc.* **443** (2014) 1211.

[136] J. Mirocha and S.R. Furlanetto, *What does the first highly redshifted 21-cm detection tell us about early galaxies?*, *Mon. Not. R. Astron. Soc.* **483** (2019) 1980.

[137] J. Mirocha, G.J.A. Harker and J.O. Burns, *Interpreting the Global 21 cm Signal from High Redshifts. I. Model-Independent Constraints*, *Astrophys. J.* **777** (2013) 118.

[138] J. Mirocha, G.J.A. Harker and J.O. Burns, *Interpreting the Global 21 cm Signal from High Redshifts. II. Parameter Estimation for Models of Galaxy Formation*, *Astrophys. J.* **813** (2015) 11.

[139] D.A. Verner, G.J. Ferland, K.T. Korista and D.G. Yakovlev, *Atomic Data for Astrophysics. II. New Analytic Fits for Photoionization Cross Sections of Atoms and Ions*, *Astrophys. J.* **465** (1996) 487.

[140] J.M. Shull and M.E. van Steenberg, *X-ray secondary heating and ionization in quasar emission-line clouds*, *Astrophys. J.* **298** (1985) 268.

[141] I. Reis, A. Fialkov and R. Barkana, *The subtlety of Ly α photons: changing the expected range of the 21-cm signal*, *Mon. Not. R. Astron. Soc.* **506** (2021) 5479.

[142] T. Theuns, A. Leonard, G. Efstathiou, F.R. Pearce and P.A. Thomas, *P^3M-SPH simulations of the Lyα forest*, *Mon. Not. R. Astron. Soc.* **301** (1998) 478.

[143] S.R. Furlanetto and S.J. Stoever, *Secondary ionization and heating by fast electrons*, *Mon. Not. R. Astron. Soc.* **404** (2010) 1869.

[144] A. Ewall-Wice, T.-C. Chang, J. Lazio, O. Doré, M. Seiffert and R.A. Monsalve, *Modeling the radio background from the first black holes at cosmic dawn: Implications for the 21 cm absorption amplitude*, *Astrophys. J.* **868** (2018) 63.

[145] A. Ewall-Wice, T.-C. Chang and T.J.W. Lazio, *The Radio Scream from black holes at Cosmic Dawn: a semi-analytic model for the impact of radio-loud black holes on the 21-cm global signal*, *Mon. Not. R. Astron. Soc.* **492** (2019) 6086.

[146] S. Mittal and G. Kulkarni, *Background of radio photons from primordial black holes*, *Mon. Not. R. Astron. Soc.* **510** (2022) 4992.

[147] S.W. Hawking, *Particle creation by black holes*, *Commun. Math. Phys.* **43** (1975) 199.

[148] D.N. Page, *Particle emission rates from a black hole: Massless particles from an uncharged, nonrotating hole*, *Phys. Rev. D* **13** (1976) 198.

[149] D.N. Page, *Particle emission rates from a black hole. II. Massless particles from a rotating hole*, *Phys. Rev. D* **14** (1976) 3260.

[150] J.H. MacGibbon and B.R. Webber, *Quark- and gluon-jet emission from primordial black holes: The instantaneous spectra*, *Phys. Rev. D* **41** (1990) 3052.

[151] J.H. MacGibbon, *Quark- and gluon-jet emission from primordial black holes. II. The emission over the black-hole lifetime*, *Phys. Rev. D* **44** (1991) 376.

[152] J.H. MacGibbon, B.J. Carr and D.N. Page, *Do evaporating black holes form photospheres?*, *Phys. Rev. D* **78** (2008) 064043.

[153] A. Arbey and J. Auffinger, *BlackHawk: a public code for calculating the Hawking evaporation spectra of any black hole distribution*, *Eur. Phys. J. C* **79** (2019) 693.

[154] H. Liu, G.W. Ridgway and T.R. Slatyer, *Code package for calculating modified cosmic ionization and thermal histories with dark matter and other exotic energy injections*, *Phys. Rev. D* **101** (2020) 023530.

[155] H. Liu, T.R. Slatyer and J. Zavala, *Contributions to cosmic reionization from dark matter annihilation and decay*, *Phys. Rev. D* **94** (2016) 063507.

[156] T.R. Slatyer, *Indirect dark matter signatures in the cosmic dark ages. II. Ionization, heating, and photon production from arbitrary energy injections*, *Phys. Rev. D* **93** (2016) 023521.

[157] P.J.E. Peebles, *Recombination of the Primeval Plasma*, *Astrophys. J.* **153** (1968) 1.

[158] Y. Ali-Haïmoud and C.M. Hirata, *HyRec: A fast and highly accurate primordial hydrogen and helium recombination code*, *Phys. Rev. D* **83** (2011) 043513.

[159] B. Ciardi and P. Madau, *Probing beyond the Epoch of Hydrogen Reionization with 21 Centimeter Radiation*, *Astrophys. J.* **596** (2003) 1.

[160] R. Hills, G. Kulkarni, P.D. Meerburg and E. Puchwein, *Concerns about modelling of the EDGES data*, *Nature* **564** (2018) E32.

[161] A. Chatterjee, T.R. Choudhury and S. Mitra, `CosmoReionMC`: *a package for estimating cosmological and astrophysical parameters using CMB, Lyman-α absorption, and global 21 cm data*, *Mon. Not. R. Astron. Soc.* **507** (2021) 2405.

[162] J. Goodman and J. Weare, *Ensemble samplers with affine invariance*, *Commun. Appl. Math. Comput. Sci.* **5** (2010) 65.

[163] D. Foreman-Mackey, D.W. Hogg, D. Lang and J. Goodman, *emcee: The MCMC hammer*, *Publ. Astron. Soc. Pac.* **125** (2013) 306.

[164] E. Bugaev and P. Klimai, *Constraints on amplitudes of curvature perturbations from primordial black holes*, *Phys. Rev. D* **79** (2009) 103511.

[165] A.S. Josan, A.M. Green and K.A. Malik, *Generalised constraints on the curvature perturbation from primordial black holes*, *Phys. Rev. D* **79** (2009) 103520.

[166] G. Sato-Polito, E.D. Kovetz and M. Kamionkowski, *Constraints on the primordial curvature power spectrum from primordial black holes*, *Phys. Rev. D* **100** (2019) 063521.

[167] A. Kalaja, N. Bellomo, N. Bartolo, D. Bertacca, S. Matarrese, I. Musco et al., *From primordial black holes abundance to primordial curvature power spectrum (and back)*, *JCAP* **2019** (2019) 031.

[168] B.J. Carr, *The Primordial Black Hole Mass Spectrum*, *Astrophys. J.* **201** (1975) 1.

[169] L. Husdal, *On Effective Degrees of Freedom in the Early Universe*, *Galaxies* **4** (2016) 78.

[170] T. Harada, C.-M. Yoo and K. Kohri, *Threshold of primordial black hole formation*, *Phys. Rev. D* **88** (2013) 084051.

A   Tables of constraints

Tables 2 and 3 list the numerical values of our constraints on $\log_{10} f_{\text{PBH}}$ shown in figure 6. These tables are also available in electronic format from the arXiv article web page.

Mass (g)	$\log_{10} f_{\text{PBH}}$
1×10^{15}	$-6.840^{+0.020}_{-0.019}$
2×10^{15}	$-5.848^{+0.011}_{-0.012}$
3×10^{15}	$-5.201^{+0.014}_{-0.014}$
4×10^{15}	$-4.672^{+0.014}_{-0.014}$
5×10^{15}	$-4.227^{+0.015}_{-0.014}$
6×10^{15}	$-3.815^{+0.011}_{-0.011}$
7×10^{15}	$-3.466^{+0.015}_{-0.015}$
8×10^{15}	$-3.141^{+0.013}_{-0.013}$
9×10^{15}	$-2.866^{+0.012}_{-0.013}$
1×10^{16}	$-2.634^{+0.013}_{-0.013}$
2×10^{16}	$-1.619^{+0.012}_{-0.012}$
3×10^{16}	$-1.178^{+0.013}_{-0.013}$
4×10^{16}	$-0.821^{+0.011}_{-0.011}$
5×10^{16}	$-0.513^{+0.010}_{-0.010}$
6×10^{16}	$-0.213^{+0.014}_{-0.014}$
7×10^{16}	$+0.083^{+0.013}_{-0.013}$

Table 2: Constraints on $\log_{10} f_{\text{PBH}}$ when no X-ray heating is present. Since PBHs are the only major heating process in this model, the EDGES measurement formally implies a detection. The best-fitting (posterior median) value of $\log_{10} f_{\text{PBH}}$ and the associated 90% confidence limits are listed. These constraints are shown graphically by the blue line in figure 6.

Mass (g)	$\log_{10} f_{\mathrm{PBH}}$
1×10^{15}	-9.729
2×10^{15}	-8.796
3×10^{15}	-8.064
4×10^{15}	-7.567
5×10^{15}	-7.108
6×10^{15}	-6.695
7×10^{15}	-6.428
8×10^{15}	-6.185
9×10^{15}	-5.748
1×10^{16}	-5.548
2×10^{16}	-4.587
3×10^{16}	-4.041
4×10^{16}	-3.626
5×10^{16}	-3.259
6×10^{16}	-2.905
7×10^{16}	-2.706
8×10^{16}	-2.512
9×10^{16}	-2.275
1×10^{17}	-1.970
2×10^{17}	-0.448
3×10^{17}	$+0.080$

Table 3: Constraints on $\log_{10} f_{\mathrm{PBH}}$ in the presence of X-ray heating. Only an upper limit on $\log_{10} f_{\mathrm{PBH}}$ is obtained in this model; we list the 95th percentile here. These constraints are shown graphically by the red line and the shaded region in figure 6.